

X-Shooter study of accretion in ρ -Ophiucus: very low-mass stars and brown dwarfs [★]

C.F. Manara^{1,★★}, L. Testi^{2,3,4}, A. Natta^{3,5}, and J. M. Alcalá⁶

¹ Scientific Support Office, Directorate of Science and Robotic Exploration, European Space Research and Technology Centre (ESA/ESTEC), Keplerlaan 1, 2201 AZ Noordwijk, The Netherlands
e-mail: cmanara@cosmos.esa.int

² European Southern Observatory, Karl Schwarzschild Str. 2, 85748 Garching bei München, Germany

³ INAF/Osservatorio Astrofisico of Arcetri, Largo E. Fermi, 5, 50125 Firenze, Italy

⁴ Excellence Cluster Universe, Boltzmannstr. 2, D-85748 Garching bei München, Germany

⁵ School of Cosmic Physics, Dublin Institute for Advanced Studies, 31 Fitzwilliams Place, 2 Dublin, Ireland

⁶ INAF/Osservatorio Astronomico di Capodimonte, Salita Moiarriello, 16 80131 Napoli, Italy

Received March, 24th 2015; accepted May, 4th 2015

ABSTRACT

We present new VLT/X-Shooter optical and near-infrared spectra of a sample of 17 candidate young low-mass stars and brown dwarfs located in the ρ -Ophiucus cluster. We derived the spectral type and extinction for all the targets, and then we determined their physical parameters. All the objects but one have $M_{\star} \leq 0.6 M_{\odot}$, and eight have mass below or close to the hydrogen-burning limit. Using the intensity of various permitted emission lines present in their spectra, we determined the accretion luminosity and mass accretion rates (\dot{M}_{acc}) for all the objects. When compared with previous works targeting the same sample, we find that, in general, these objects are not as strongly accreting as previously reported, and we suggest that the reason is our more accurate estimate of the photospheric parameters. We also compare our findings with recent works in other slightly older star-forming regions, such as Lupus, to investigate possible differences in the accretion properties, but we find that the accretion properties for our targets have the same dependence on the stellar and substellar parameters as in the other regions. This leads us to conclude that we do not find evidence for a different dependence of \dot{M}_{acc} with M_{\star} when comparing low-mass stars and brown dwarfs. Moreover, we find a similar small ($\lesssim 1$ dex) scatter in the $\dot{M}_{\text{acc}}-M_{\star}$ relation as in some of our recent works in other star-forming regions, and no significant differences in \dot{M}_{acc} due to different ages or properties of the regions. The latter result suffers, however, from low statistics and sample selection biases in the current studies. The small scatter in the $\dot{M}_{\text{acc}}-M_{\star}$ correlation confirms that mass accretion rate measurements in the literature based on uncertain photospheric parameters and single accretion indicators, such as the $H\alpha$ width, can lead to a scatter that is unphysically large. Our studies show that only broadband spectroscopic surveys coupled with a detailed analysis of the photospheric and accretion properties allows us to properly study the evolution of disk accretion rates in star-forming regions.

Key words. Stars: pre-main sequence – stars: formation – brown dwarfs – protoplanetary disks – accretion, accretion disks – open clusters and associations: individual: ρ -Ophiucus

1. Introduction

The evolution of protoplanetary disks surrounding forming stars has been a major subject of study in recent years. The interest in this topic is driven by the fact that disks are the birthplace of planets. A clear understanding of the physical mechanisms driving the formation, evolution, and dispersal of disks is thus needed to constrain planet formation theories, and to explain the observed properties of our own solar system and of the wealth of exoplanetary systems discovered so far.

During their evolution, the central young stellar object (YSO) and the surrounding disk interact through multiple processes, such as photoevaporation, stellar winds, and accretion of matter. The latter is a result of viscous processes happening in the disk, which drive its secular evolution (e.g., Hartmann et al., 1998), while photoevaporation and winds/outflows are thought to play a major role in the final disk dispersal (e.g., Alexander et al., 2014, and references therein). A good understanding of these

processes is needed to describe how disks evolve, and thus how planet formation takes place. Star-disk interaction processes can be studied observationally through the strong signatures they introduce in the spectra of YSOs. Accretion shocks give rise to continuum excess emission in the UV (e.g., Valenti et al., 1993; Gullbring et al., 1998, 2000; Calvet & Gullbring, 1998; Calvet et al., 2000) and the prominent emission of permitted lines across the whole spectrum (e.g., Muzerolle et al., 1998a,b,c, 2003; Natta et al., 2004), while winds are traced by various forbidden emission lines (e.g., Hartigan et al., 1995; Rigliaco et al., 2013; Natta et al., 2014). In recent years, new instruments have provided the possibility of studying these processes simultaneously in large samples of objects. In particular, the X-Shooter spectrograph mounted on the ESO/VLT telescope (Vernet et al., 2011) provides us the possibility of studying YSOs with unprecedented levels of detail, as it simultaneously takes spectra at medium resolution ($R \sim 5000-20000$) over the complete wavelength range from ~ 300 nm to ~ 2500 nm. We are thus able to study all the signatures of accretion and winds in the optical and near-infrared spectra of YSOs at the same time.

[★] This work is based on observations made with ESO Telescopes at the Paranal Observatory under programme ID 085.C-0876.

^{★★} ESA Research Fellow

A significant effort has been made recently to study YSOs with X-Shooter. The accretion process has been studied for objects located in various nearby star-forming regions (σ -Ori, Rigliaco et al. 2012; Lupus, Alcalá et al. 2014; Chamaeleon, Manara et al. 2015) and at various phases of disk evolution (e.g., transitional disks; Manara et al., 2014). These works, among various results, showed that the mass accretion rates (\dot{M}_{acc}) dependence on the stellar mass (M_*) has a significant smaller scatter (~ 0.4 dex) than previously observed (Alcalá et al., 2014), and that there are transitional disks with comparable accretion rates as less evolved disks (Manara et al., 2014). These works focused on very low-mass, pre-main-sequence (PMS) stars and up to solar mass YSOs, with only a few objects below the hydrogen burning limit (e.g., Rigliaco et al., 2011b; Stelzer et al., 2013). These objects were located in regions with age ~ 2 -3 Myr, or more. However, to fully test models of disk evolution it is important to derive accretion properties of YSOs for a large range of stellar masses and age. The work we present here aims to enlarge the sample of very low-mass stars (VLMS) and brown dwarfs (BDs) studied with X-Shooter, focusing on objects located in the younger (age ~ 1 Myr) ρ -Oph embedded cluster.

The ρ -Oph cluster is located at a distance $d \sim 125$ pc (Lombardi et al., 2008; Loinard et al., 2008), and it is still highly embedded in the parental cloud, with values of A_V up to 50 mag in the densest core (Wilking & Lada, 1983), and with a rather high value of total-to-selective extinction ratio $R_V \sim 5.6$ (e.g., Kenyon et al., 1998; Chapman et al., 2009; McClure et al., 2010; Comerón et al., 2010). The total population of the surrounding Ophiucus region is estimated to be of around 300 YSOs (Evans et al., 2009), with ~ 200 YSOs located in ρ -Oph itself. Given the large quantity of YSOs present in this cluster and its proximity, it has been extensively studied in the past at various wavelengths from optical, near- and far-infrared, millimeter, radio, to X-ray (e.g., Greene & Meyer, 1995; Luhman & Rieke, 1999; Wilking et al., 2005; Alves de Oliveira et al., 2010, 2012, 2013; Bontemps et al., 2001; McClure et al., 2010; Gagné et al., 2004).

Various works aimed to understand the accretion properties of YSOs at early ages have targeted ρ -Oph. In particular, Natta et al. (2006, hereafter N06) have studied the vast majority of the Class II YSOs in this cluster, selected from the ISO sample of Bontemps et al. (2001). They used near-infrared emission lines (Pa β and Bry) to determine the accretion rates, and a statistical approach, based on the assumption that the whole population is located on the Hertzsprung-Russell diagram (HRD) on a single isochrone at 0.5 Myr, to derive stellar parameters for most of the targets¹. This work showed that accretion rates for BDs in ρ -Oph are typically higher than for objects with the same mass in Taurus, and that various strongly accreting BDs are found in this region. However, this result strongly depends on the already mentioned assumptions, which can result in incorrect estimates of the stellar parameters, extinction, or accretion for single objects, and only more precise analyses can shed light on this issue. With the set of X-Shooter spectra we present here, we are able to derive stellar and accretion parameters with significantly higher precision. With this in hand, we aim at addressing the still open questions comparing accretion properties for BDs and VLMS in this region and in other samples observed with X-Shooter.

The paper is organized as follows. In Section 2 we describe the sample, observations, and data reduction; in Section 3 we then discuss the method used to analyze the spectra and the derived properties of the objects, together with their main spectral features. In Section 4 we determine the accretion properties of the targets, and discuss the differences with previous estimates for the same targets; the comparison of accretion properties with results from other regions is then carried out in Section 5. Finally, we discuss our findings and conclusions in Section 6.

2. Sample, observations, and data reduction

We report here about new data collected with the ESO/VLT X-Shooter spectrograph (Vernet et al., 2011) during Pr.Id.085.C-0876 (PI Testi). This instrument acquires spectra of the targets from $\lambda \sim 300$ nm to $\lambda \sim 2500$ nm simultaneously, splitting the spectrum in three parts, usually referred to as the UVB ($\lambda \sim 300$ -550 nm), VIS ($\lambda \sim 550$ -1050 nm), and NIR ($\lambda \sim 1050$ -2500 nm) arms.

The sample was selected from the one of N06 to cover as many of the objects with detected accretion and estimated stellar mass $M_* < 0.1 M_\odot$ as possible. It comprises 16 Class II YSOs and one Class I YSO that are analyzed here for the first time, one transitional disk (ISO-Oph196) that has been analyzed in Manara et al. (2014), and three Class III YSOs. We focus on the analysis of the 16 Class II YSOs and the Class I YSO. All these targets were included in the ISO sample compiled by Bontemps et al. (2001) and most of them have previously been studied spectroscopically (e.g., Natta et al., 2002, 2004, 2006; Wilking et al., 1999, 2005, see also Table A.1 for literature data on these targets). Their ISO number, other names, and coordinates are reported in the first three columns of Table 1.

All the objects have been observed in service mode using the $1.0 \times 11''$ slit in the UVB arm and the $0.9 \times 11''$ slits in the VIS and NIR arms, which lead to a nominal resolution $R = \lambda/\Delta\lambda \sim 4350, 7450$, and 5300 in the three arms, respectively. Different exposure times have been adopted for each target depending on their estimated fluxes. The dates of the observations and exposure times are reported in the fourth and fifth columns of Table 1. The late spectral type (SpT) of most of the targets and the high extinction of the region explain the low SNR of most spectra, at least in the UVB arm. The only spectra with any detected signal in the continuum in the UVB arm are those of ISO-Oph032 and ISO-Oph123, although with low SNR. Some objects have also very low SNR in the VIS spectra at $\lambda \lesssim 600$ -700 nm, or even at longer wavelengths. The NIR spectra of all targets have a good SNR. We report the SNR for the various spectra at different wavelengths in the last three columns of Table 1. The object ISO-Oph072 was reported by McClure et al. (2010) to be member of a binary system with a separation of $3.62''$. The X-Shooter spectrum analyzed here is the one of the primary component of the system, while the secondary was not included in the slit.

Data reduction has been carried out using the X-Shooter pipeline (Modigliani et al., 2010) version 1.3.7 and the same procedure as in Alcalá et al. (2014). For the targets observed on 2010-06-01, 2010-08-20, and 2010-08-28, the photometric standard observed during the night of observation is not supported anymore in the pipeline. The flux calibration of the spectra has thus been obtained using the photometric standard star observed the following night, which was always photometric. The flux calibration of the spectra reduced with the pipeline has been compared with available 2MASS photometry and rescaled to this using synthetic photometry on the spectra to match the photometric flux. The correction factors are larger than 1 and usually

¹ Their results were obtained using an old distance estimate of 160 pc, and have been corrected for the newly determined distance and recalculated with the same method, but assuming a single isochrone at 1 Myr for the whole population by Rigliaco et al. (2011a). Here we report in Tables D.1 all the values derived using the most recent distance estimated for the cluster of 125 pc.

Table 1. Sample, observing log, and SNR of the spectra

Object/other name	RA(2000) h : m : s	DEC(2000) ° ' "	Obs. date YY-MM-DD	Exp. Time [s]	SNR at $\lambda =$		
					700	855	1300
ISO-Oph023 / SKS1	16:26:18.821	-24:26:10.52	2010-08-20	4×750s	0	4	61
ISO-Oph030 / GY5	16:26:21.528	-24:26:00.96	2010-08-20	4×750s	15	71	66
ISO-Oph032 / GY3	16:26:21.899	-24:44:39.76	2010-06-01	4×750s	12	29	65
ISO-Oph033 / GY11	16:26:22.269	-24:24:07.06	2010-08-26	4×1800s	0	2	29
ISO-Oph037 / LFAM3 / GY21	16:26:23.580	-24:24:39.50	2010-08-21	4×750s	0	2	36
ISO-Oph072 / WL18	16:26:48.980	-24:38:25.24	2010-04-06	4×480s	3	17	51
ISO-Oph087	16:26:58.639	-24:18:34.66	2010-08-28	4×750s	0	2	29
ISO-Oph094	16:27:03.591	-24:20:05.45	2010-08-28	4×750s	0	1	10
ISO-Oph102 / GY204	16:27:06.596	-24:41:48.84	2010-07-23	4×750s	12	41	68
ISO-Oph115 / WL11 / GY229	16:27:12.131	-24:34:49.14	2010-07-30	4×750s	0	1	37
ISO-Oph117 / WLY2-32b / GY235	16:27:13.823	-24:43:31.66	2010-06-08	4×480s	3	17	92
ISO-Oph123	16:27:17.590	-24:05:13.70	2010-08-27	4×750s	58	74	83
ISO-Oph160 / B162737-241756	16:27:37.422	-24:17:54.87	2010-08-27	4×750s	1	15	62
ISO-Oph164 / GY310	16:27:38.631	-24:38:39.19	2010-06-08	4×750s	6	31	45
ISO-Oph165 / GY312	16:27:38.945	-24:40:20.67	2010-06-08	4×750s	0	1	27
ISO-Oph176 / GY350	16:27:46.291	-24:31:41.19	2010-08-21	4×750s	1	16	89
ISO-Oph193 / B162812-241138	16:28:12.720	-24:11:35.60	2010-08-21	4×750s	2	28	24

Notes. Exposure times are the same in the three X-Shooter arms (UVB, VIS, and NIR). Wavelengths for the SNR calculation are reported in nm.

lower than ~ 1.5 , and always less than ~ 1.9 . Indeed, these spectra have all been obtained with slits whose sizes are comparable with the seeing, so the slit losses are small. The only spectrum in which the conjunctions between spectra from different arms are not very good is ISO-Oph102. In this object, the quality of the spectrum in the last ~ 100 nm of the VIS arm is not good, and this results in a bad matching of the VIS and NIR arms. Finally, telluric line removal has been performed using the IRAF² task *telluric* following the procedure discussed in Alcalá et al. (2014) and using standard telluric spectra obtained close in time and air mass to the targets.

3. Stellar and substellar properties

Here we discuss the method adopted to derive the stellar and substellar properties of the targets, and also the results obtained and main features present in the spectra.

3.1. Method

Spectral classification for objects located in ρ -Oph is a difficult process, as these are usually highly-extincted and large excess because of disk emission, is also present at near-IR wavelengths (e.g., Luhman & Rieke, 1999; Wilking et al., 2005; Natta et al., 2006). Thanks to the very large wavelength coverage of our spectra, however, we can derive the spectral type (SpT) and extinction (A_V) of the targets using multiple spectral features simultaneously, thus reducing the degeneracies present in this analysis. Given that the spectra have very low or zero SNR in the UVB arm, the analysis cannot be performed using the method described in Manara et al. (2013b), which simultaneously determines SpT, A_V , and accretion luminosity (L_{acc}), fitting the UV and visible part of the spectra with a grid of models that includes the contribution of photospheric and accretion-induced emission, and reddening. Similarly, the analysis methods used by

Table 2. Grid of photospheric templates

Object	SpT	T_{eff} [K]	Ref
TWA9A	K5	4350	1
TWA6	K7	4060	1
TWA25	M0	3850	1
TWA14	M0.5	3780	1
TWA13B	M1	3705	1
synthetic spectrum	M1.5	3600	2
Sz122	M2	3560	1
synthetic spectrum	M2.5	3500	2
TWA7	M3	3415	1
TWA15A	M3.5	3340	1
Sz94	M4	3270	1
SO797	M4.5	3200	1
Par-Lup3-2	M5	3125	1
SO999	M5.5	3060	1
synthetic spectrum	M6	3000	2
Par-Lup3-1	M6.5	2935	1
synthetic spectrum	M7	2900	2
synthetic spectrum	M7.5	2800	2
synthetic spectrum	M8	2700	2
synthetic spectrum	M8.5	2550	2
TWA26	M9	2400	1
TWA29	M9.5	2330	1
synthetic spectrum	L0	2200	2

References. 1. Manara et al. (2013a); 2. Allard et al. (2011)

Alcalá et al. (2014) or Rigliaco et al. (2012) cannot be adopted here, as all these need to perform a fit of the excess in the UV part of the spectrum to derive L_{acc} , and are well suited for the SpT determination only for objects with low extinction.

The procedure we use here is the following: We collect a grid of photospheric templates, which cover the SpT from K5 to L0, with a typical step of 0.5 spectral subclasses throughout the entire M subclass. These are chosen primarily from the Class III spectra of Manara et al. (2013a), which are observed spectra of nonaccreting PMS stars obtained with the same instrument. As this grid of templates is incomplete for SpT later than M6.5 and earlier than M9, and has no spectra with SpTs M1.5, M2.5, and

² IRAF is distributed by National Optical Astronomy Observatories, which is operated by the Association of Universities for Research in Astronomy, Inc., under cooperative agreement with the National Science Foundation.

M6, to complete our grid we make use of the synthetic spectra BT-Settl of Allard et al. (2011), which are smoothed to match the resolution of the X-Shooter spectra. We adopt synthetic spectra with values of $\log g = 3.5$ (in cgs units), typical of young objects in ρ -Oph (e.g., Comerón et al., 2010), and effective temperatures (T_{eff}), corresponding to the given SpT according to the SpT- T_{eff} relation of Luhman et al. (2003). The details of the adopted grid of templates is reported in Table 2. The synthetic spectra reproduce well, in general, the observed templates down to $T_{\text{eff}} \sim 3050$ K, i.e., SpT \sim M5.5, while there are some discrepancies at lower temperatures. This, unfortunately, is also the region of our observed template library, which has a sparse sampling of spectral types. We describe the typical reddening toward the objects with the reddening law of Cardelli et al. (1989) using a value of $R_V = 5.6$.

For each target, we find the stellar parameters (SpT, A_V) with an automatic procedure that compares the observed spectrum to the various templates, which are artificially reddened (A_V ranges from 0 to 18 mag in step of 0.1 mag) and then normalized to the observed spectrum at $\lambda \sim 1025$ nm. The comparison is done between the value of the mean flux across a window of ~ 4 nm in 28 different points of the spectrum from $\lambda \sim 700$ nm to $\lambda \sim 1725$ nm, which cover various molecular features particularly strong in the spectra of VLMS and BDs and sensitive to T_{eff} , such as TiO, VO, and other molecular features (see Manara et al., 2013a, for a list) in the VIS arm, and H₂O bands in the NIR arm. We limit our comparison to points within the aforementioned spectral range to avoid regions with large veiling due to accretion and low SNR spectra due to high extinction ($\lambda < 700$ nm), and regions where the contribution of the disk emission is substantial ($\lambda \gtrsim 1700$ nm). The best fit is derived by minimizing a χ^2_{like} distribution, similar to the procedure by Manara et al. (2013b), on the two free parameters SpT and A_V . This is defined as

$$\chi^2_{\text{like}} = \sum_i \left(\frac{f_{\text{obs}}(\lambda_i) - f_{\text{mod}}(\lambda_i)}{\sigma_{\text{obs}}(\lambda_i)} \right)^2, \quad (1)$$

where the index i denotes the various points included in the analysis, f_{obs} is the flux of the observed spectrum, f_{mod} that of the template, and σ_{obs} is the standard deviation on the flux of the observed spectrum. Uncertainties in the estimated parameters (SpT, A_V) are derived from the $\Delta\chi^2_{\text{like}}$ distribution, considered as a $\Delta\chi^2$ distribution. Points where the SNR on the observed target is less than 5 are excluded from the χ^2_{like} calculation. To have enough SNR in the VIS arm, we use spectra smoothed using the *boxcar smoothing* procedure included in the IRAF *splot* package. This procedure convolves the spectrum with a rectangular box, whose width we set to 7 pixels, and results in a broadening of the narrower absorption and emission lines and features, but preserves their fluxes and equivalent widths. The results of the fit do not change using the smoothed spectra, but only the uncertainties on the results and the numbers of points included in the fit. At the same time, the different resolution of the templates does not influence the result of the fit, as all the points where the χ^2_{like} is calculated are free of narrow absorption lines. We also include a constraint on the accepted fits, namely that the observed spectrum should have a larger flux than the template at $\lambda > 2115$ nm, i.e., in the K-band, a part of the spectrum not used otherwise in the analysis.

Various checks have been carried out on this procedure to determine its reliability, which we list here: *i*) Starting from our own grid of templates, we artificially add to their spectra various amounts of veiling due to accretion, of emission from the

disk, and of reddening due to extinction. By applying the procedure just described in most cases we retrieve their correct stellar parameters. These stellar parameters only have big discrepancies in cases where the veiling due to accretion is substantial, i.e., the ratio of accretion to stellar luminosity (L_{acc}/L_\star) is larger than 0.5. This is expected to be the case for very few low-mass Class II YSOs (e.g., Alcalá et al., 2014). *ii*) We fit several X-Shooter spectra of Class II YSOs in Lupus by Alcalá et al. (2014) and retrieve results compatible with theirs, similarly to case *i*, as these objects are not strongly veiled. *iii*) We run our procedure using only synthetic spectra for the later type objects or varying the resolution of the synthetic spectra. These different grids generally lead to differences in the derived parameters well within their uncertainties. *iv*) We try to use spectra smoothed both in the VIS and NIR arms, while in general we smoothed only the VIS arm, and we obtain small differences. *v*) We try to use only non-smoothed spectra, with which we get similar results, but with larger uncertainties.

The method just described allows us to derive SpT and A_V for all targets and lead to good best fits. We show in Appendix B (Figs. B.1 – B.6) the reddening corrected spectra with their best-fit template, also including additional *Spitzer* photometry from the literature. The values of $\chi^2_{\text{like,red}} = \chi^2_{\text{like}}/d.o.f.$ range from ~ 0.5 to ~ 3 , with only two objects, ISO-Oph102 and ISO-Oph123, with $\chi^2_{\text{like,red}} > 4$ (see Appendix A for further discussion on these objects). We adopt a slightly different approach for the two objects with larger veiling due to accretion in our sample, ISO-Oph072 and ISO-Oph123. For these two targets we exclude from the χ^2_{like} calculation all the points at $\lambda > 1340$ nm, i.e., in the *H*-band. This choice is made as we expect that strongly accreting objects make a significant contribution to the emission at near-IR wavelengths from a disk, which is not included in our modeling. With this choice, we obtain the same result for ISO-Oph123 as with the inclusion of all the points in the χ^2_{like} calculation, but with a lower value of $\chi^2_{\text{like,red}}$. As we discuss in the following, the results for ISO-Oph123 are highly uncertain and the derived stellar properties for this object should be used with caution. For ISO-Oph072, instead we derive a significantly later SpT (M3.5 instead of K7), but with a significantly smaller value of $\chi^2_{\text{like,red}}$ (2.2 instead of 4.7). We check the results also excluding the *H*-band for objects with strong infrared excess due to an envelope, such as ISO-Oph037 and ISO-Oph165 (see Table A.1 and Figs. B.1-B.6). For both of these targets, we derive A_V and SpT within the uncertainties of the normal procedure including all the points. However, as fewer points are included in the fit, the statistical significance of the results is lower. We decide then to use the values obtained using all points in the fit for these two objects, as well.

3.2. Derived properties

The stellar parameters derived from the best-fit results are reported in Table 3 with their 1σ uncertainties. The first two panels of Fig. 1 show the histograms of the SpT and A_V derived for our targets. The vast majority of the YSOs in our sample are of M-type SpT, with 7 out of 17 targets having SpT M6.5 or later. The derived values of A_V are in the range from ~ 0 mag to ~ 16 mag, and with a uniform distribution in this interval. We compare our findings with those in the literature in Sect. 3.3.

From the best-fit parameters (SpT, A_V) we derive T_{eff} using the SpT- T_{eff} relation of Luhman et al. (2003). Stellar luminosity (L_\star) is derived from the ratio of the flux of the reddening corrected observed spectrum to the flux of the best-fit template

Table 3. Spectral types, extinction, and physical parameters of the ρ -Oph Class II YSOs

Object	SpT	T_{eff} [K]	A_V [mag]	L_* [L_{\odot}]	R_* [R_{\odot}]	M_* [M_{\odot}]
ISO–Oph023	M7	2900 $^{+85}_{-50}$	9.7 $^{+0.2}_{-0.1}$	0.040 $^{+0.017}_{-0.002}$	0.79 \pm 0.20	0.07 $^{+0.02}_{-0.01}$
ISO–Oph030	M7	2900 $^{+50}_{-50}$	4.5 $^{+0.2}_{-0.1}$	0.067 $^{+0.003}_{-0.000}$	1.03 \pm 0.04	0.10 $^{+0.01}_{-0.01}$
ISO–Oph032	M6.5	2935 $^{+50}_{-50}$	0.6 $^{+0.1}_{-0.1}$	0.033 $^{+0.000}_{-0.000}$	0.70 \pm 0.03	0.07 $^{+0.01}_{-0.01}$
ISO–Oph033	M8	2700 $^{+150}_{-50}$	7.7 $^{+0.4}_{-0.2}$	0.005 $^{+0.001}_{-0.000}$	0.32 \pm 0.06	0.03 $^{+0.02}_{-0.01}$
ISO–Oph037	K7	4060 $^{+50}_{-50}$	16.1 $^{+0.1}_{-0.2}$	0.415 $^{+0.000}_{-0.017}$	1.31 \pm 0.21	1.02 $^{+0.01}_{-0.01}$
ISO–Oph072*	M3.5	3340 $^{+50}_{-50}$	8.2 $^{+0.2}_{-0.1}$	0.106 $^{+0.005}_{-0.004}$	0.97 \pm 0.04	0.30 $^{+0.01}_{-0.01}$
ISO–Oph087	M4.5	3200 $^{+50}_{-50}$	13.3 $^{+0.1}_{-0.2}$	0.109 $^{+0.000}_{-0.005}$	1.08 \pm 0.05	0.22 $^{+0.01}_{-0.01}$
ISO–Oph094†	M1.5	3600 $^{+50}_{-235}$	10.0 $^{+0.8}_{-0.1}$	0.009 $^{+0.003}_{-0.001}$	0.25 \pm 0.06	0.40
ISO–Oph102	M5	3125 $^{+50}_{-50}$	2.2 $^{+0.1}_{-0.1}$	0.047 $^{+0.000}_{-0.000}$	0.74 \pm 0.02	0.15 $^{+0.01}_{-0.01}$
ISO–Oph115	M2	3560 $^{+50}_{-110}$	15.1 $^{+0.1}_{-0.7}$	0.145 $^{+0.006}_{-0.035}$	1.00 \pm 0.14	0.51 $^{+0.01}_{-0.07}$
ISO–Oph117	M3.5	3340 $^{+50}_{-50}$	9.1 $^{+0.1}_{-0.1}$	0.221 $^{+0.000}_{-0.000}$	1.41 \pm 0.04	0.33 $^{+0.01}_{-0.01}$
ISO–Oph123*	K7**	4060**	4.3**	0.078**	0.56**	0.62**
ISO–Oph160	M7.5	2800 $^{+50}_{-50}$	6.1 $^{+0.1}_{-0.2}$	0.030 $^{+0.000}_{-0.001}$	0.73 \pm 0.03	0.06 $^{+0.01}_{-0.01}$
ISO–Oph164	M8	2700 $^{+50}_{-50}$	5.1 $^{+0.2}_{-0.1}$	0.052 $^{+0.002}_{-0.000}$	1.05 \pm 0.05	0.05
ISO–Oph165†	M2.5	3500 $^{+150}_{-135}$	12.1 $^{+0.6}_{-0.2}$	0.034 $^{+0.011}_{-0.001}$	0.50 \pm 0.10	0.40 $^{+0.08}_{-0.08}$
ISO–Oph176	M7.5	2800 $^{+50}_{-50}$	6.9 $^{+0.1}_{-0.1}$	0.057 $^{+0.000}_{-0.000}$	1.02 \pm 0.04	0.06
ISO–Oph193	M6	3000 $^{+50}_{-50}$	7.4 $^{+0.2}_{-0.2}$	0.072 $^{+0.003}_{-0.003}$	1.00 \pm 0.07	0.11 $^{+0.01}_{-0.01}$

Notes. M_* are derived using the evolutionary tracks of Baraffe et al. (1998). * Object with strong veiling due to accretion. ** These stellar parameters are very uncertain and should be used with caution. See Appendix A for a discussion on this target. † Subluminous YSOs. M_* reported with no uncertainties are for objects whose location on the HRD is at the edge of the tabulated evolutionary tracks.

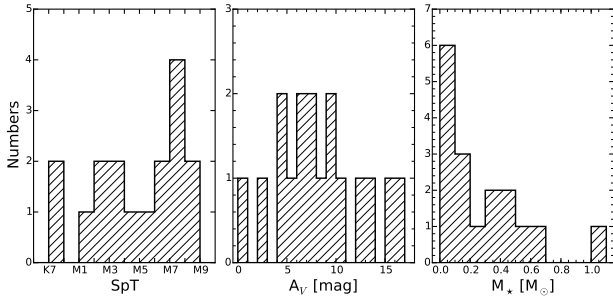


Fig. 1. Histograms of the properties of the targets. The left-hand panel shows the SpTs, the middle panel shows the A_V , and the right-hand panels shows the M_* . According to M_* derived using Baraffe et al. (1998) evolutionary tracks, the sample comprises six BDs and two objects with mass just at the hydrogen-burning limit.

at $\lambda \sim 1025$ nm (K) and the known parameters of the template. In particular, when the best-fit template is a Class III YSO, we know its L_* and distance (Manara et al., 2013a), so we can determine L_* for our target simply considering the squared ratio of the distances and the ratio K of the two spectra, as in Manara et al. (2013b). On the other hand, when the best-fit template is a synthetic spectrum, L_* is simply the total flux of the synthetic spectrum rescaled at the distance of ρ -Oph and multiplied by K , i.e., $L_* = 4\pi \cdot d_{\rho\text{-Oph}}^2 \cdot K \cdot F_{\text{tot,template}}$, which is a similar procedure as in Alcalá et al. (2011, and references therein). Stellar radii (R_*) are derived from the relation $L_* = 4\pi R_*^2 \sigma_B T^4$, while M_* from

comparison of the position of the targets on the HRD with the evolutionary tracks by Baraffe et al. (1998). We also show the distribution of M_* for our targets in the right-hand panel of Fig. 1. According to the parameters derived with the Baraffe et al. (1998) evolutionary tracks, six objects in our sample have a mass below the hydrogen-burning limit (ISO–Oph023, ISO–Oph032, ISO–Oph033, ISO–Oph160, ISO–Oph164, and ISO–Oph176), and two more have a value of M_* close to this limit ($M_* \sim 0.1 M_{\odot}$, ISO–Oph030 and ISO–Oph193). The majority of the YSOs have $M_* \leq 0.6 M_{\odot}$, and only one object has $M_* \sim 1 M_{\odot}$.

The position of the targets on the HRD is shown in Fig. 2, together with the 1σ (red lines) and 3σ uncertainties (blue lines) on the estimated parameters. An additional $\lesssim 0.2$ dex uncertainty on L_* should be considered, as this is the error on the luminosity of the templates due to uncertainties in the distance and in the flux calibration of the spectra (e.g., Manara et al., 2013a; Alcalá et al., 2014). The HRD is shown with two different sets of evolutionary tracks, those by Baraffe et al. (1998, upper panel) and those by D’Antona & Mazzitelli (1994, bottom panel). The majority of the targets (14 out of 17) is found to be located on the HRD at positions compatible with young (< 5 –10 Myr) ages according to both sets of models, and at ages $\lesssim 3$ Myr according to D’Antona & Mazzitelli (1994) evolutionary tracks. The latter set of models appears to reproduce better the positions on the HRD of the BDs in the sample, in particular, of ISO–Oph176 and ISO–Oph164. We however adopt the parameters derived using the evolutionary tracks from Baraffe et al. (1998) for consistency with previous studies of accretion in nearby star-forming regions (e.g., Alcalá et al., 2014).

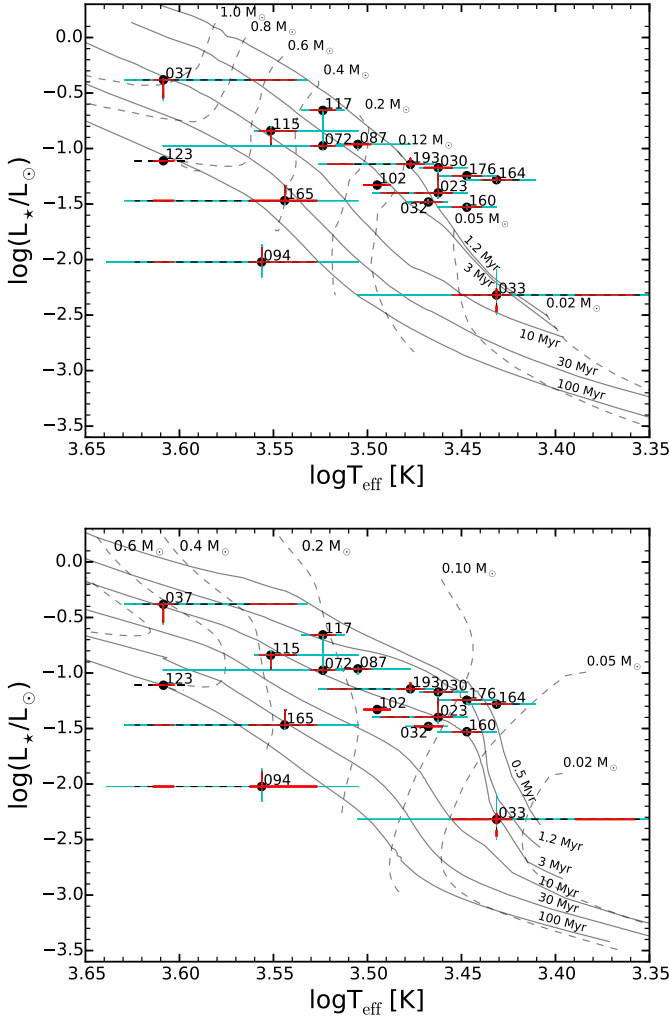


Fig. 2. Hertzsprung-Russell diagram for the ρ -Oph Class II YSOs analyzed here. The continuous lines show the isochrones, while the dashed lines show the low-mass pre-main sequence evolutionary tracks. The upper panel is obtained using the tracks by Baraffe et al. (1998), while the bottom panel with tracks by D’Antona & Mazzitelli (1994). ISO numbers are reported for all the objects. Red lines represent the 1σ error on the parameters, while cyan lines the 3σ one. The objects ISO–Oph094 and ISO–Oph165 are classified as being subluminoous probably due to an edge-on disk for the former and to a still partly optically thick envelope in the latter, which is a Class I target. The stellar parameters and the position on the HRD of ISO–Oph123 is very uncertain due to the very strong veiling due to accretion, which makes the spectral classification extremely difficult.

For three objects (ISO–Oph123, ISO–Oph165, and ISO–Oph094) the position on the HRD is significantly closer to the main sequence, thus suggesting an older age than the rest of the targets. However, none of these targets are probably really old. The first object, ISO–Oph123, is extremely veiled and this makes it difficult to detect the photospheric continuum. Therefore, the stellar parameters for this target are very uncertain. We discuss this case in detail in Appendix A. Regarding ISO–Oph165, mid-infrared data have shown that this object is still embedded in its own parental envelope, and it is classified as a Class I YSO (McClure et al., 2010). For this reason, the stellar parameters are uncertain, A_V is high, and an erroneously

lower stellar luminosity estimate is possible. Finally, we suggest that ISO–Oph094 is a target whose circumstellar disk is edge-on, as its spectrum has an almost undetected continuum, also with a very low SNR in the NIR arm. We note that distance uncertainties for these objects are probably not leading to an erroneous location on the HRD, as a factor of ~ 2.5 larger distance would be needed to position ISO–Oph165 closer to the bulk of the population, and this factor is even higher (~ 5) for ISO–Oph094. For the remainder of this work, we refer to ISO–Oph165 and ISO–Oph094 as subluminoous YSOs and use a different symbol in the plots to differentiate these from the other targets. Additional information and discussion on these objects is given in Appendix A.

3.3. Comparison with previous results

Most of the targets analyzed here have been previously observed in near-infrared spectroscopic or photometric studies (e.g., Wilking et al., 1999; Luhman & Rieke, 1999; Natta et al., 2002, 2004, 2006) or with optical spectroscopy (e.g., Wilking et al., 2005). The stellar parameters (SpT, A_V) derived in these works for our targets are reported in Table A.1 and in Table D.1 for N06.

The comparison between the SpTs derived here and those obtained with spectroscopy in the literature (Table A.1) is shown in Fig. 3, where all the literature estimates are reported using circles for the most recent one and crosses for the older results. All our SpT estimates agree within 1 or 2 spectral sub-classes with previous studies, with the only two exceptions being ISO–Oph123, which was classified as M3.5, while we find a very uncertain best fit with SpT K7, and ISO–Oph072, which we found to have a SpT M3.5, while it was previously classified as K6.5 by Wilking et al. (2005). In both cases, the targets are strongly veiled, and thus their spectral type classification is subject to large uncertainties that can justify these differences. Finally, we derive for ISO–Oph117 a SpT of M3.5, which is in better agreement with the SpT M5 reported by McClure et al. (2010) than with the SpT K8 found by Gatti et al. (2006).

According to N06, only four objects in our sample should have M_\star well above the hydrogen burning limit (ISO–Oph037, ISO–Oph072, ISO–Oph087, and ISO–Oph117). The result of our analysis confirms that all these YSOs are VLMS. At the same time, among the other 13 targets that were classified as BDs in N06 only 8 are confirmed as BDs by our analysis, if we also consider ISO–Oph030 and ISO–Oph193 as BDs. Three more targets that were classified as BDs are those with highly uncertain stellar parameters, as they are either subluminoous (ISO–Oph094, ISO–Oph165) or strongly veiled (ISO–Oph123). Regarding the remaining two objects that were thought to be BDs, we classify ISO–Oph102 as of M5 SpT and with a M_\star slightly above the hydrogen-burning limit ($M_\star = 0.15 M_\odot$), and this estimate is also compatible with Wilking et al. (2005). Finally, our derived M_\star for ISO–Oph115 is $0.5 M_\odot$, while it was reported to be just above the hydrogen burning limit by N06. However, this object was reported to have a SpT M0 by other authors (Gatti et al., 2006; McClure et al., 2010), which confirms it is a low-mass YSO, not a BD.

In Fig. 4 we show the comparison between the values of A_V derived here with those derived by N06 for all the objects in our sample (cyan squares) and by other works for most of the targets (black circles). We see that most values agree within a typical difference up to ~ 1 mag. The largest differences are found for ISO–Oph165, where both N06 and McClure et al. (2010) report a value of $A_V \sim 15$ –17 mag higher than our estimate $A_V = 12$.

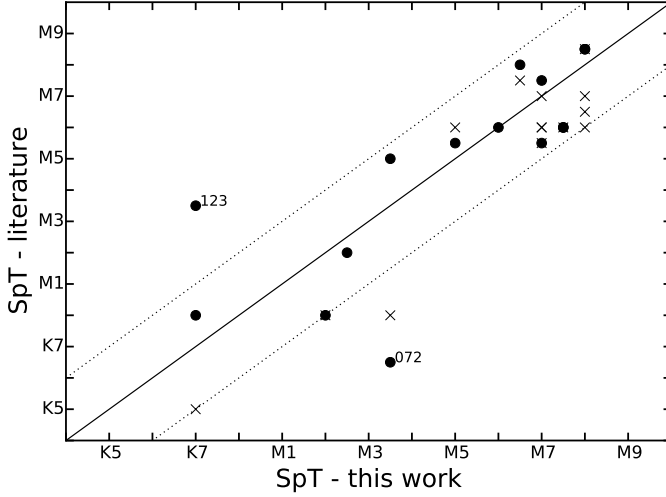


Fig. 3. Comparison of the SpT derived here for the targets (Sect. 3.2) with those reported in the literature (see Table A.1 for the references). Black circles report the most recent SpT estimate found in the literature, while black crosses are used for other SpT estimates available. The dotted lines show the ± 2 spectral subclasses difference between the two values. The larger discrepancies are for ISO–Oph123, classified here as K7 except with very uncertain parameters, and ISO–Oph072, which we classify as M3.5, and was reported to be K6.5 in the literature.

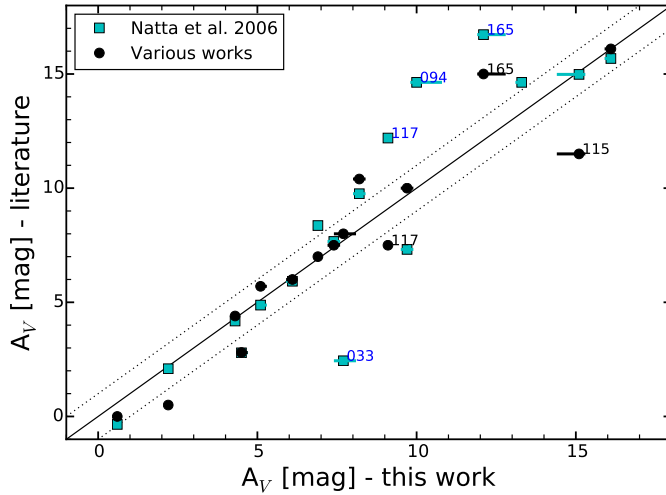


Fig. 4. Comparison of the A_V derived here for the targets (Sect. 3.2) with those reported in the literature. The latter are shown with *cyan squares* in the case of values derived by N06 and in *black circles* when from other works (see Table A.1 for the references). The dotted lines show the ± 1 mag difference between the two values. One sigma uncertainties in our estimates are reported, and are sometimes smaller than the symbol.

mag, and then for ISO–Oph094, reported to have $A_V=14.6$ mag by N06 and found to have $A_V=10$ mag here. In one case the derived value differs from the estimates of N06 but not with other studies (ISO–Oph033) or viceversa (ISO–Oph115), while the differences of A_V derived for ISO–Oph117 are higher than 2 mag with all previous studies, but in different directions.

Finally, we compare the L_\star derived here with those determined by N06 and modified to account for the correct distance

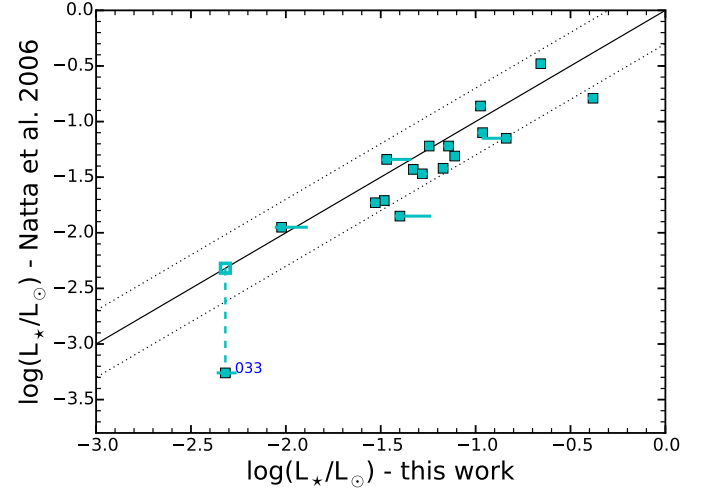


Fig. 5. Comparison of the L_\star derived here for the targets (Sect. 3.2) with those from N06 and corrected for distance as discussed by Rigliaco et al. (2011a). The dotted lines show a difference between the L_\star values of a factor 2. The only object with a significantly larger difference is ISO–Oph033, but its L_\star has been revised by Comerón et al. (2010) and the latter value, in agreement with ours, is reported with an empty symbol. One sigma uncertainties in our estimates are reported, and are sometimes smaller than the symbol.

estimate (see Table D.1). This is a very interesting comparison, as L_\star is derived with two independent methods. Therefore, it is very important to note that the two methods lead to similar results for all targets, with differences smaller than a factor ~ 2 . The only exception is ISO–Oph033, but we note that the revised analysis by Comerón et al. (2010) leads to the same value of L_\star as the value we derived here.

To summarize, we find, in most cases, values for A_V and L_\star to be compatible with those by N06 and other literature studies, but that the derived M_\star differ from the literature estimate. The main reason for the different estimates of M_\star is the different T_{eff} determined here with a more robust method than those by N06 and with better data than most previous spectroscopic studies.

3.4. Spectral features

We visually investigate the spectra with $\text{SNR} > 10$ in the continuum at ~ 700 nm for the presence of the Li I absorption line at $\lambda 670.78$ nm, a known proxy of youth in YSOs. We clearly detect this line in the spectrum of ISO–Oph032, while it is only tentatively detected in the spectra of ISO–Oph030, ISO–Oph102, and ISO–Oph123. In the latter, the SNR of the spectrum is very high, but the strong veiling makes all the absorption lines very weak. For all these targets, we report the presence of lithium for the first time, while the low SNR of the other spectra hinder the detection of this line in the rest of the sample.

Various permitted emission lines are detected in the spectra of our targets, and these are used in the next section to derive the accretion luminosity of the targets. In few spectra with high SNR, we also detect forbidden emission lines. In particular, the [OI] $\lambda 6300$ Å line is detected in the spectra of ISO–Oph030, ISO–Oph032, ISO–Oph102, and ISO–Oph123. The analysis of these lines is out of the scope of this paper and will be discussed in a following work.

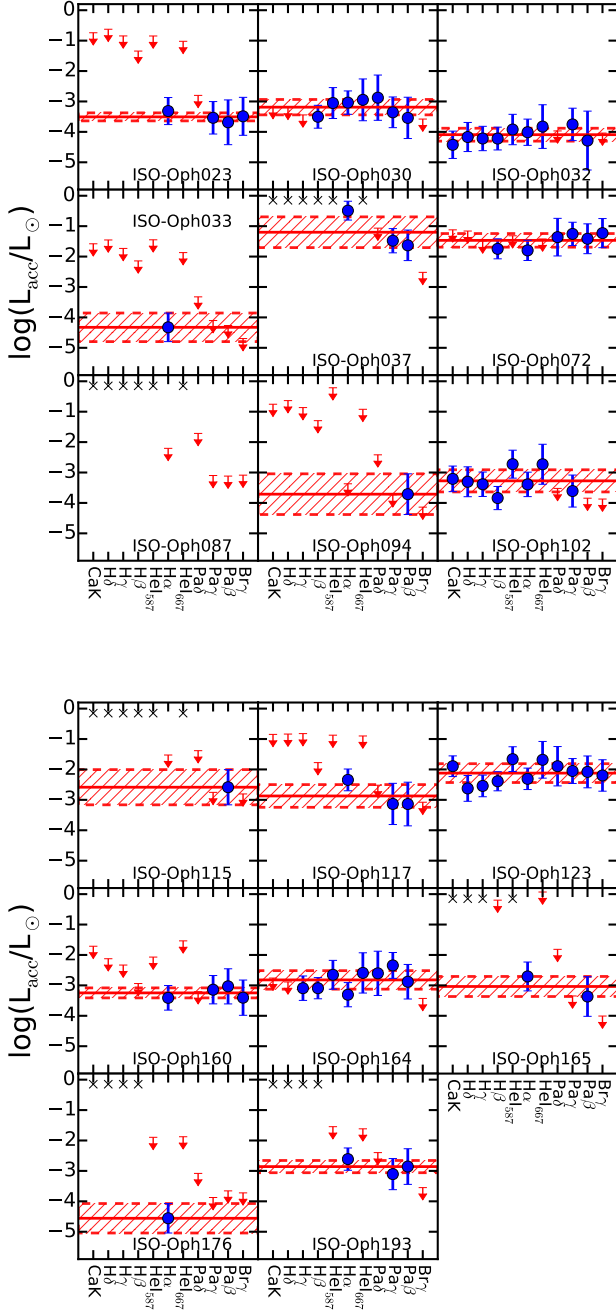


Fig. 6. Accretion luminosity derived from various emission lines luminosity for the ρ -Oph targets. Each subplot shows the value of $\log(L_{\text{acc}}/L_{\odot})$ derived using the various indicators reported on the x-axis (CaK, H δ , H γ , H β , He $_{\lambda 587\text{nm}}$, H α , He $_{\lambda 667\text{nm}}$, Pa δ , Pa γ , Pa β , Br γ) and in order of increasing wavelength. The red solid line is the average values obtained from the detected lines, while the dashed lines are the 1σ standard deviation of this value. Black crosses are for upper limits out of the range of the plot, i.e., larger than $\log(L_{\text{acc}}/L_{\odot}) \sim -0.1$. As upper limits depend on the rms noise of the spectra, they are significantly higher than measurements when the SNR is low, in particular, in the UVB arm.

4. Accretion properties of ρ -Ophiucus young stellar objects

The accretion luminosity for our targets is derived using relations between the luminosity of emission lines (L_{line}) and L_{acc} , which have been calibrated by Alcalá et al. (2014). These represent the only suitable way to determine L_{acc} from our spectra, as the UV-excess is not detected in the spectra because of the high extinction of the region. This is an indirect method that is less accurate than direct fitting of the UV-excess, but it has been shown that L_{acc} determined in this way are consistent with direct measurements of L_{acc} when multiple lines are used (e.g., Rigliaco et al., 2012; Alcalá et al., 2014).

For this analysis, we then select 11 emission lines that are usually bright and whose L_{line} has a good correlation with L_{acc} , namely CaK, H δ , H γ , H β , He $_{\lambda 587\text{nm}}$, H α , He $_{\lambda 667\text{nm}}$, Pa δ , Pa γ , Pa β , Br γ . We determine the flux of the emission lines from the flux-calibrated and extinction-corrected spectra using an automatic Python procedure that determines the value of the continuum and the extent of the line, which is then directly integrated with no additional modeling. All the line extent determination of the automatic procedures are checked by eye, and the derived flux of the lines are compatible with results obtained using different methods, such as direct integration using the *splot* package under IRAF. The error on the line flux is obtained propagating the 1σ standard deviation on the continuum flux over the integration window. For nondetected lines, we calculate the 3σ upper limits with the relationship $3 \times F_{\text{noise}} \times \Delta\lambda$, where F_{noise} is the rms flux-noise in the region of the line and $\Delta\lambda$ is the expected average line width, assumed to be 0.2 nm. The fluxes and equivalent width (EW) of the lines, together with their respective errors, are reported in Table C.1.

All the objects analyzed here with detected H α line have $\text{EW}_{\text{H}\alpha}$ well above the threshold for accretors reported by White & Basri (2003), and thus are confirmed accretors. This line is not detected in the spectra of ISO-Oph087, ISO-Oph094, and ISO-Oph115, which have $\text{SNR} \sim 0$ on the continuum adjacent to the line. For the latter target, we are able to determine L_{acc} from the Pa β line and this leads to a value above the chromospheric noise level, i.e., the intensity of the chromospheric emission in a nonaccreting YSO, determined by Manara et al. (2013a) for objects with this T_{eff} . The value of L_{acc} determined for ISO-Oph094 from the luminosity of the Pa β line seems compatible with pure chromospheric emission. However, this object is probably observed edge-on, thus the measured line intensity is probably only a lower limit of the real line intensity. Finally, no emission lines are detected for ISO-Oph087, which could then possibly be a nonaccreting YSO.

The luminosity of the lines is calculated as $L_{\text{line}} = 4\pi d^2 \cdot f_{\text{line}}$, where d is the distance of ρ -Oph and f_{line} the flux of the line. The value of L_{acc} is then determined as the average of the values of L_{acc} determined from the $L_{\text{acc}}-L_{\text{line}}$ relations from the detected lines, while the error is the standard deviation of these values. Figure 6 shows the values of L_{acc} determined with each line for all the targets. The accretion luminosity for the targets are reported in the second column of Table 4, while the number of detected emission lines used to calculate L_{acc} is available in the last column of the same table. We estimate an upper limit on L_{acc} for ISO-Oph187 from the upper limit on the H α line and use this value in the analysis.

Finally, \dot{M}_{acc} is determined from the values of L_{acc} just obtained and from the stellar parameters M_{\star} and R_{\star} determined as explained in the previous section. These parameters are related by the relation $\dot{M}_{\text{acc}} = 1.25 \cdot L_{\text{acc}} R_{\star} / (GM_{\star})$ (e.g., Hartmann et

Table 4. Accretion luminosity and mass accretion rates of the ρ -Oph YSOs

Object	$\log L_{\text{acc}}$ [L_{\odot}]	$\log \dot{M}_{\text{acc}}$ [M_{\odot}/yr]	Detected lines [#]
ISO-Oph023	-3.51	-9.85	4
ISO-Oph030	-3.19	-9.58	7
ISO-Oph032	-4.09	-10.49	9
ISO-Oph033	-4.33	-10.70	1
ISO-Oph037	-1.20	-8.49	3
ISO-Oph072	-1.47	-8.36	8
ISO-Oph087	<-2.21	<-8.92	0
ISO-Oph094	-3.71	-11.32	1
ISO-Oph102	-3.27	-9.98	8
ISO-Oph115	-2.58	-9.69	1
ISO-Oph117	-2.87	-9.64	3
ISO-Oph123	-2.12	-9.56	11
ISO-Oph160	-3.25	-9.56	4
ISO-Oph164	-2.82	-8.90	8
ISO-Oph165	-3.04	-10.34	2
ISO-Oph176	-4.60	-10.73	1
ISO-Oph193	-2.86	-9.30	3

Notes. L_{acc} is obtained as the mean of the values from the different emission lines. \dot{M}_{acc} are derived using \dot{M}_{\star} determined from the evolutionary tracks of Baraffe et al. (1998). The last column reports the number of emission lines detected and used to derive L_{acc} .

al., 1998), which assumes accretion from a radius $R_m = 5R_{\star}$. The final value is reported for every object in the third column of Table 4.

4.1. Comparison with previous results

The most comprehensive catalog of accretion rates in ρ -Oph was compiled by N06. Here we compare the accretion properties we derived for our sample with the accretion properties compiled by N06 for the same objects. As already mentioned in Sect. 3.3, the results may differ in particular on the estimates of T_{eff} and \dot{M}_{\star} due to the different methodologies. Indeed, \dot{M}_{acc} depends on various stellar parameters (\dot{M}_{\star} , R_{\star} , thus L_{\star} and T_{eff}), which have been determined here with a more detailed analysis. As we reported in Sect. 1, N06 did not have estimates for the SpT for most of the targets and had to assume that they were located on the HRD on a single isochrone after determining L_{\star} from the infrared colors. Our estimates of L_{\star} are consistent with those of N06, except that the T_{eff} estimated by N06 may differ substantially from ours in many cases, up to the extreme cases of the subluminoous objects, which could not be classified as such by N06 given their methodological assumption. This results in different \dot{M}_{\star} and R_{\star} between the two works. Moreover, N06 use the intensity of a single emission line to derive L_{acc} , while we measure this quantity using multiple, up to 11, emission lines. We are thus less affected by scatter in one single $L_{\text{acc}}-L_{\text{line}}$ relation or by other processes that modify the intensity of a single line.

We first show in Fig. 7 the comparison of the $L_{\text{acc}}-L_{\star}$ relation for the objects included in our sample using our own results (black points) and those from N06 (red symbols). The two distributions appear very similar, with the majority of the points located between the $L_{\text{acc}}=0.1 L_{\star}$ and $L_{\text{acc}}=0.01 L_{\star}$ lines. In general, most of the targets are located very close to the $L_{\text{acc}}=0.01 L_{\star}$ line, with slightly smaller dispersion than in the previous work reported here. This is also the case for the two subluminoous targets, which appear on this plot in the same position

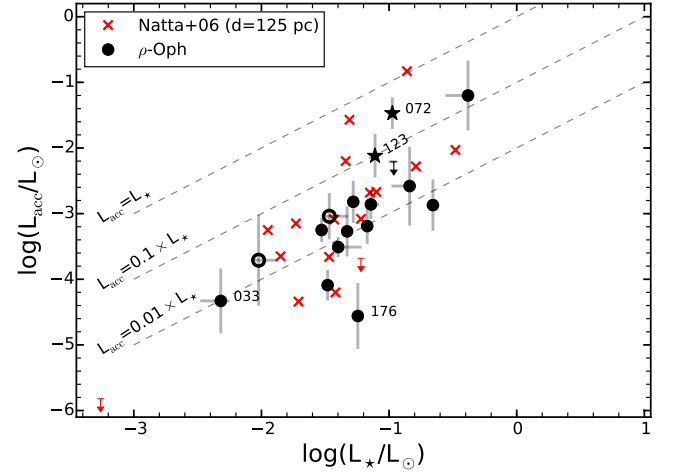


Fig. 7. Comparison of accretion rate luminosity as a function of stellar luminosity for our sample with data from N06 for the same targets. Values from N06 are shown with red crosses, while our results with black circles. Empty black circles are used for subluminoous targets and downward arrows for upper limits. Dashed lines are for different L_{acc}/L_{\star} ratios, going downward from 1, to 0.1, to 0.01, as labeled. The object most to the left-hand side of the plot in both samples is ISO-Oph033.

as the rest of the YSOs. The value of L_{\star} we determine here for ISO-Oph033 (bottom left point in both samples) is larger than that by N06, as discussed earlier, leading to a position of this target on the $L_{\text{acc}}-L_{\star}$ plane closer to the bulk of the population than before. The object with the lower L_{acc}/L_{\star} ratio is ISO-Oph176, but its L_{acc} is still compatible with a line intensity being genuinely due to accretion, and not to chromospheric emission. Finally, the position of ISO-Oph123 on the $L_{\text{acc}}=0.1 L_{\star}$ line is probably due to the already discussed uncertainties in its parameters. In reality, because of its strong emission, both in lines and continuum, this object is expected to fall closer to the $L_{\text{acc}}=L_{\star}$ line in this diagram, as it was according to N06. Appendix A provides further discussion on this target.

The comparison of our measurements of \dot{M}_{acc} with those by N06 is shown in Fig. 8, where we plot the $\log \dot{M}_{\text{acc}}$ vs $\log \dot{M}_{\star}$ values for the objects analyzed here, again using the black symbols for our results and red symbols for those by N06. With respect to the results of N06, the largest discrepancies are in the derived \dot{M}_{\star} , which in many cases are larger in our work. This is a consequence of the later SpT determined for various objects with respect to those assumed by N06 (see discussion in Sect. 3.3). At the same time, the range of values of \dot{M}_{acc} is similar for the two works, but our estimates lead to a smaller number of strongly accreting BDs than those of N06. In particular, all the objects in our sample with reliable (sub)stellar and accretion parameters are found on the $\dot{M}_{\text{acc}}-\dot{M}_{\star}$ to follow the best-fit relation found by Alcalá et al. (2014, shown here with a solid gray line within its dispersion, indicated with dashed lines), while $\sim 50\%$ of these targets were above this region for N06. The only object in our sample significantly above the dispersion of the best-fit relation by Alcalá et al. (2014) is ISO-Oph164. For this target, \dot{M}_{\star} remains similar to that derived by N06, while \dot{M}_{acc} increases by more than an order of magnitude. This object appears to have a L_{\star} slightly higher than the rest of the objects analyzed here with similar SpT (see Fig. 2), and this could lead to a slightly higher \dot{M}_{acc} . The only targets that are located on the $\dot{M}_{\text{acc}}-\dot{M}_{\star}$

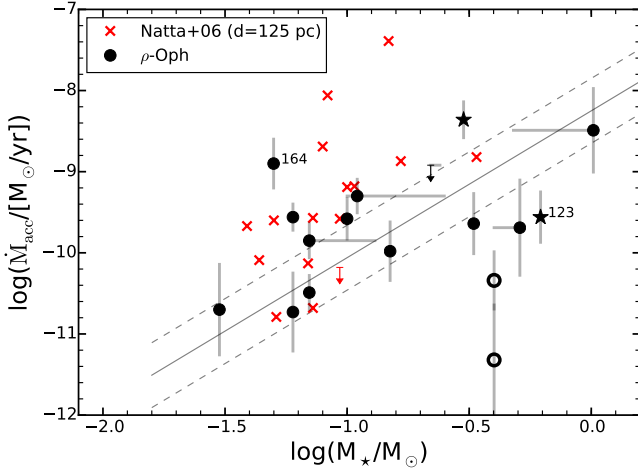


Fig. 8. Mass accretion rate as a function of mass for the ρ -Oph sample. Values derived for the objects analyzed here are reported with black markers, values from N06 are shown with red symbols. Empty black circles are used for subluminal targets and downward arrows are used for upper limits. The continuous line represents the linear fit of this relation by Alcalá et al. (2014) for a sample of accreting objects in Lupus. The dashed lines represent the 1σ deviation from the fit.

plane significantly below the bulk of the population are the two subluminal targets.

We can thus conclude from this analysis that, in our limited sample of BDs and VLMS, we see a smaller number of heavily accreting targets than N06. This strongly suggests that BDs and VLMS in ρ -Oph accrete at a rate similar to those in other regions, as we discuss in the next section, contrary to the claim of N06. As the typical L_{acc}/L_* ratio in our targets is similar to that determined by N06, our suggestion is that the differences in the $\dot{M}_{\text{acc}}-M_*$ relation is mostly because of the different (sub)stellar parameters determined here. Given that we do not have assumptions about the positions of the targets on the HRD, and we have larger wavelength coverage that lead to a better constraint of A_V , SpT, and L_* , we are confident that our results are more reliable and that the distribution we observe in the $\dot{M}_{\text{acc}}-M_*$ plane for our sample resembles the real distribution. A larger study on the whole sample of N06 with a data set similar to ours would further reinforce our finding. At present we do not attempt to fit our results as we have few objects sparsely sampled in the parameter space (L_* , L_{acc} , M_* , \dot{M}_{acc}).

5. Accretion in ρ -Oph compared with nearby star-forming regions

As discussed in Sect. 1, the main interests in the data set presented here are to determine whether BDs in ρ -Oph have significantly higher accretion rates than in other star-forming regions, and to study a very young region to compare the accretion properties of its targets with those of targets located in older star-forming regions. We have just discussed how our results differ from those of N06 in the $\dot{M}_{\text{acc}}-M_*$ plane, leading to lower accretion rates for BDs than those reported by them. Here we compare our findings with those of Alcalá et al. (2014) in the Lupus I and III clouds, and those by Rigliaco et al. (2012) in the σ -Orionis (σ -Ori) cluster. These are selected as comparison sample as they include a significant number of VLMS and some (~ 5) BDs, and

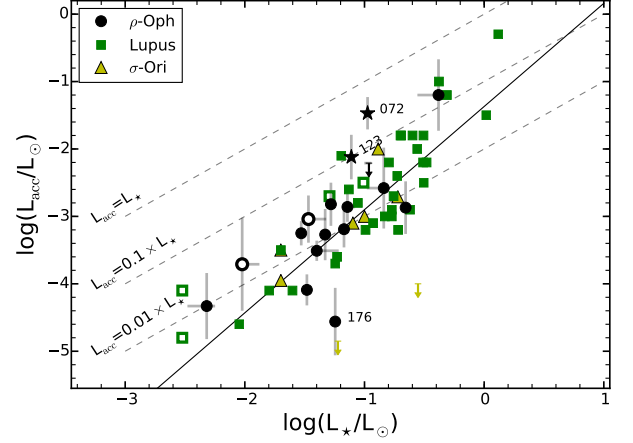


Fig. 9. Accretion luminosity vs stellar luminosity for the whole ρ -Oph sample discussed here (black symbols), for the Lupus sample of Alcalá et al. (2014), reported with green symbols, and for a sample in σ -Ori studied by Rigliaco et al. (2012) and reported with yellow triangles. Upper limits are shown as downward arrows. Empty symbols are used for subluminal objects, and stars for strongly veiled objects. Dashed lines are for different L_{acc}/L_* ratios, going downward from 1, to 0.1, to 0.01, as labeled. The solid lines is the best fit for the GTO sample by Natta et al. (2014).

have been studied using spectra obtained with the same instrument. In addition, our accretion rates are determined using the $L_{\text{acc}}-L_{\text{line}}$ relation determined from these samples, hence the biases in the \dot{M}_{acc} estimates are minimized than when comparing \dot{M}_{acc} estimates with other data sets. As these data have been collected as part of the Italian guaranteed time observation (GTO; Alcalá et al., 2011), in the following we refer to the whole comparison sample as GTO sample. Our targets are also interesting as they enlarge the number of targets at low M_* , in particular, there are six more BDs and two more objects with M_* just at the hydrogen burning limit.

5.1. Accretion luminosity and stellar luminosity relation

We show in Fig. 9 the position of our targets and those from the GTO sample (cf. legend in the plot and caption for symbols explanations) in the $L_{\text{acc}}-L_*$ plane. This is a particularly interesting relation as it is obtained independently from models of PMS evolution, thus it can be considered a “purely observational” plot. The plot also indicates the best-fit relation for the GTO sample by Natta et al. (2014), in which the slope is 1.53 ± 0.18 .

All the targets analyzed here are located in the same part of the $L_{\text{acc}}-L_*$ plane as those from the GTO sample. In particular, we do not have any extremely strong accretors ($L_{\text{acc}}/L_* > 0.5$), with the only possible exception being ISO-Oph123, which is probably more intensely accreting than what is reported here. The number of objects between the $L_{\text{acc}} = 0.01 L_*$ and $L_{\text{acc}} = 0.1 L_*$ lines decreases drastically at $L_* \leq 0.1 L_\odot$ in the GTO sample, and the same appears to be true in our sample, as well. Also for this reason the best-fit relation has a slope significantly steeper than unity, implying that for higher luminosity targets the emission due to accretion is relatively more important than in lower L_* objects. This is also confirmed by the data collected here.

The location of the two subluminal targets in our sample is similar to that of subluminal targets in the GTO sample (empty

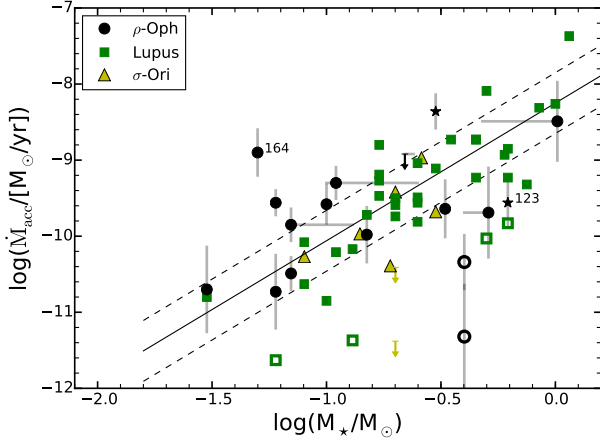


Fig. 10. Mass accretion rate as a function of mass for the whole ρ -Oph sample discussed here (black symbols) and for the Lupus sample of Alcalá et al. (2014), reported with green symbols. Upper limits are shown as downward arrows. Symbols are as in Fig. 9. The continuous line represents the linear fit of this relation for the Lupus sample (Alcalá et al., 2014), and the dashed lines represent the 1σ deviation from the fit.

symbols in the plot). Similar to what was found by Alcalá et al. (2014) for the four subluminescent targets reported here, we find that they appear in the upper boundary of the points in the $L_{\text{acc}}-L_{\star}$ plane.

Finally, our sample does not widen the spread on the $L_{\text{acc}}-L_{\star}$ plane with respect to that found with the GTO sample. This suggests that the small spread in this relation found by Alcalá et al. (2014) is not particular to the Lupus clouds, but is probably also common in other star-forming regions and is obtained when the data are analyzed with homogeneous methods.

5.2. Accretion as a function of stellar mass

We present the values of $\log \dot{M}_{\text{acc}}$ vs $\log \dot{M}_{\text{acc}}$ for our and the GTO samples (cf. caption and legend for explanation of the symbols) in Fig. 10, together with the best-fit relation derived by Alcalá et al. (2014) for the Lupus sample alone. The latter has a slope of 1.8 ± 0.2 and is particularly interesting as it is based on a large sample, but has a very small scatter ($\sigma = 0.4$ dex) from the best-fit relation compared to previous studies (e.g., Muzerolle et al., 2003; Mohanty et al., 2005; Natta et al., 2006; Herczeg & Hillenbrand, 2008; Rigliaco et al., 2011a; Manara et al., 2012). Our sample does not substantially broaden the scatter of \dot{M}_{acc} at any M_{\star} , whereas most targets appear to be consistent with the best fit of the $\dot{M}_{\text{acc}}-M_{\star}$ relation and its dispersion. Only a couple of BDs and the two objects with M_{\star} close to the hydrogen-burning limit in our sample seem to have a value of \dot{M}_{acc} at the upper edge of the dispersion from the best-fit relation reported by Alcalá et al. (2014). However, the only one well above this relation is ISO-Oph164, which, as discussed earlier, has a slightly higher L_{\star} than objects with similar SpT. This suggests that BDs in ρ -Oph are not significantly stronger accretors than those in other star-forming regions, if they are strong accretors at all. As the majority of our targets follow the best-fit relation of Alcalá et al. (2014), we then suggest that the scaling of \dot{M}_{acc} with M_{\star} is the same for VLMS and BDs. This relation is also independent of environmental conditions, as it is confirmed by our data

based on targets located in a region with higher density than in the Lupus clouds.

As in the Lupus sample, the objects classified here as sub-luminous (empty symbols in the plot) are located in the $\dot{M}_{\text{acc}}-M_{\star}$ plane below the others. However, these objects are probably edge-on disks, thus they do not imply that the spread is larger as their stellar and accretion parameters cannot be constrained properly with our spectra.

Assuming that the slope of the $\log \dot{M}_{\text{acc}}-\log M_{\star}$ relation is ~ 1.8 , we find that this is slightly shallower than that predicted by Padoan et al. (2005) from models of Bondy-Hoyle accretion onto the forming YSO. This slope is instead the same as predicted by Dullemond et al. (2006) assuming specific initial conditions, i.e., a small spread of angular momentum of cores at the first stages of star formation. The small spread of \dot{M}_{acc} at any M_{\star} found by Alcalá et al. (2014), and also present in this sample, would also suggest that the initial conditions at formation are similar for these objects. As one of the stronger predictions from the latter work is a very tight $\dot{M}_{\text{acc}}-M_{\text{disk}}$ relation, we await future ALMA studies coupled with large samples of objects with reliably determined stellar and accretion properties for a further confirmation of their theory. On the other hand, various studies suggested that the $\dot{M}_{\text{acc}}-M_{\star}$ relation is mostly a result of the evolution of disks under the effects of photoevaporation (e.g., Clarke & Pringle, 2006; Ercolano et al., 2014). If this is the case, then our results seem to favor models of X-ray driven photoevaporation, which predict a slope of $\sim 1.5-1.7$ (Ercolano et al., 2014), with respect to those of EUV driven photoevaporation, predicting much shallower slopes of ~ 1.35 (Clarke & Pringle, 2006). As discussed also by Alcalá et al. (2014) for the Lupus sample alone, there is in the data analyzed here no evidence of the double power-law behavior suggested by Vorobyov & Basu (2009), and the apparent bimodality of past data could be ascribed to mixing \dot{M}_{acc} determined with different methods and evolutionary models. Finally, the upper envelope of our measurements has a slope similar to the bulk of the population and steeper than 1, contrary to the prediction of Hartmann et al. (2006), which describes the $\dot{M}_{\text{acc}}-M_{\star}$ relation as a consequence of layered disk accretion. To further constrain models using this relation, it is necessary to apply methods similar to those used for the GTO sample or to the method described here when the UV-excess is not detectable, to analyze larger and complete samples of data to avoid poor statistics. A strong caveat to this discussion is, however, that the exact value of the slope is uncertain and depends on several parameters. In particular, the choice of the evolutionary model used to derive M_{\star} is crucial, as this can lead to different slopes, and even to different spread of \dot{M}_{acc} . Here we have elected to use one evolutionary model (Baraffe et al., 1998) to have results compatible with past analyses, but our results on the $\dot{M}_{\text{acc}}-M_{\star}$ relation can be model-dependent.

Finally, we do not see in our objects, in comparison with the GTO sample, any clear evidence of dependence of \dot{M}_{acc} with the age of the regions. As just discussed, the objects analyzed here and those in the GTO are roughly located in the same position on the $\dot{M}_{\text{acc}}-M_{\star}$ plane. This, however, can be the result of various effects. First of all, according to the similarity solution models by Hartmann et al. (1998), one should expect ~ 0.5 dex difference in the values of \dot{M}_{acc} for objects with similar M_{\star} and with age of 1 Myr or 3 Myr. This value is comparable with the uncertainties on our \dot{M}_{acc} estimates, and with the spread of values observed in a given star-forming region. Then, it is also possible that an age spread of few Myr is present in the ages of objects located in the same star-forming region. This would flatten any difference in \dot{M}_{acc} that might, in fact, be there. Therefore, we can only aim

to constrain the dependence of \dot{M}_{acc} with the age of the targets with significantly larger samples and more reliable estimates for the PMS stellar age.

6. Conclusions

We presented new observations of 17 VLMS and BDs with disks located in the ρ -Oph cluster. The spectra analyzed here were obtained with the VLT/X-Shooter instruments and were usually of good quality from ~ 750 nm to ~ 2500 nm, allowing us to determine SpT and A_V for our targets by comparing the spectra in various molecular features with a set of photospheric templates. With this analysis, we determined the (sub)stellar parameters for all the targets. The total sample comprises six BDs, two objects with M_\star close to the hydrogen burning limit, eight VLMS and low-mass YSOs, and one solar-mass PMS star.

We determined the accretion properties for the whole sample using the intensity of the emission lines present in our spectra and compared our findings with the most complete work available in this field (N06). Our results differ from those by N06 as we find a smaller number of strong accretors, in particular, in the BD regime. This suggests that BDs in this region are not accreting at a higher rate than in other star-forming regions, contrary to previous suggestions.

A further constraint on this result comes from the comparison of our results with those in the Lupus clouds by Alcalá et al. (2014) and in the σ -Ori cluster by Rigliaco et al. (2012), the GTO sample. Our objects follow the same $L_{\text{acc}}-L_\star$ and $\dot{M}_{\text{acc}}-M_\star$ relations as those in the GTO sample. However, these findings are based on very few objects.

Finally, we do not find any evidence of differences of the accretion properties of targets located in the young (~ 1 Myr) ρ -Oph cluster or in the older (~ 3 Myr) regions targeted in the GTO survey. However, the differences expected are small and have various effects, such as observational uncertainties and age spread, and can make this analysis even more complicated. On the other hand, this work and other recent works that have used the capabilities of the VLT/X-Shooter spectrograph together with detailed analysis techniques (e.g., Rigliaco et al., 2012; Alcalá et al., 2014; Manara et al., 2014) have shown that the observational uncertainties in the estimates of accretion rates and the spread of values can be significantly reduced with respect to the past. This suggests that it will be possible with complete samples in various star-forming regions to have a clear understanding of the evolution of accretion with time and with the properties of the central PMS star.

Acknowledgements. We thank the anonymous referee for her/his careful reading of the manuscript. We thank the ESO staff in Paranal for performing the observations in service mode.

References

Alcalá, J. M., Stelzer, B., Covino, E., et al. 2011, *Astronomische Nachrichten*, 332, 242
 Alcalá, J. M., Natta, A., Manara, C. F., et al. 2014, *A&A*, 561, A2
 Alexander, R., Pascucci, I., Andrews, S., Armitage, P., & Cieza, L. 2014, *Protostars and Planets VI*, 475
 Allard, F., Homeier, D., & Freytag, B. 2011, *Astronomical Society of the Pacific Conference Series*, 448, 91
 Alves de Oliveira, C., Moraux, E., Bouvier, J., et al. 2010, *A&A*, 515, A75
 Alves de Oliveira, C., Moraux, E., Bouvier, J., & Bouy, H. 2012, *A&A*, 539, A151
 Alves de Oliveira, C., Ábrahám, P., Marton, G., et al. 2013, *A&A*, 559, AA126
 Baraffe, I., Chabrier, G., Allard, F., & Hauschildt, P. H. 1998, *A&A*, 337, 403
 Bontemps, S., André, P., Kaas, A. A., et al. 2001, *A&A*, 372, 173
 Calvet, N., & Gullbring, E. 1998, *ApJ*, 509, 802

Calvet, N., Hartmann, L., & Strom, S. E. 2000, in *Protostars and Planets IV*, 377
 Cardelli, J. A., Clayton, G. C., & Mathis, J. S. 1989, *ApJ*, 345, 245
 Chapman, N. L., Mundy, L. G., Lai, S.-P., & Evans, N. J., II 2009, *ApJ*, 690, 496
 Clarke, C. J., & Pringle, J. E. 2006, *MNRAS*, 370, L10
 Comerón, F., Testi, L., & Natta, A. 2010, *A&A*, 522, A47
 D'Antona, F., & Mazzitelli, I. 1994, *ApJS*, 90, 467
 Dullemond, C. P., Natta, A., & Testi, L. 2006, *ApJ*, 645, L69
 Ercolano, B., Mayr, D., Owen, J. E., Rosotti, G., & Manara, C. F. 2014, *MNRAS*, 178
 Evans, N. J., II, Dunham, M. M., Jørgensen, J. K., et al. 2009, *ApJS*, 181, 321
 Gagné, M., Skinner, S. L., & Daniel, K. J. 2004, *ApJ*, 613, 393
 Gatti, T., Testi, L., Natta, A., Randich, S., & Muzerolle, J. 2006, *A&A*, 460, 547
 Gullbring, E., Hartmann, L., Briceno, C., & Calvet, N. 1998, *ApJ*, 492, 323
 Gullbring, E., Calvet, N., Muzerolle, J., & Hartmann, L. 2000, *ApJ*, 544, 927
 Greene, T. P., & Meyer, M. R. 1995, *ApJ*, 450, 233
 Hartigan, P., Edwards, S., & Ghandour, L. 1995, *ApJ*, 452, 736
 Hartmann, L., Calvet, N., Gullbring, E., & D'Alessio, P. 1998, *ApJ*, 495, 385
 Hartmann, L., D'Alessio, P., Calvet, N., & Muzerolle, J. 2006, *ApJ*, 648, 484
 Herczeg, G. J., & Hillenbrand, L. A. 2008, *ApJ*, 681, 594
 Kenyon, S. J., Lada, E. A., & Barsony, M. 1998, *AJ*, 115, 252
 Loinard, L., Torres, R. M., Mioduszewski, A. J., & Rodríguez, L. F. 2008, *ApJ*, 675, L29
 Lombardi, M., Lada, C. J., & Alves, J. 2008, *A&A*, 480, 785
 Luhman, K. L., & Rieke, G. H. 1999, *ApJ*, 525, 440
 Luhman, K. L., Stauffer, J. R., Muench, A. A., et al. 2003, *ApJ*, 593, 1093
 Manara, C. F., Robberto, M., Da Rio, N., et al. 2012, *ApJ*, 755, 154
 Manara, C. F., Testi, L., Rigliaco, E., et al. 2013a, *A&A*, 551, A107
 Manara, C. F., Beccari, G., Da Rio, N., et al. 2013, *A&A*, 558, A114
 Manara, C. F., Testi, L., Natta, A., et al. 2014, *A&A*, 568, AA18
 Manara, C. F., Fedele, D., & Herczeg, G., in prep.
 McClure, M. 2009, *ApJ*, 693, L81
 McClure, M. K., Furlan, E., Manoj, P., et al. 2010, *ApJS*, 188, 75
 Modigliani, A., Goldoni, P., Royer, F., et al. 2010, *Proc. SPIE*, 7737
 Mohanty, S., Jayawardhana, R., & Basri, G. 2005, *ApJ*, 626, 498
 Muzerolle, J., Calvet, N., & Hartmann, L. 1998a, *ApJ*, 492, 743
 Muzerolle, J., Hartmann, L., & Calvet, N. 1998b, *AJ*, 116, 455
 Muzerolle, J., Hartmann, L., & Calvet, N. 1998c, *AJ*, 116, 2965
 Muzerolle, J., Hillenbrand, L., Calvet, N., Briceño, C., & Hartmann, L. 2003, *ApJ*, 592, 266
 Natta, A., Testi, L., Comerón, F., et al. 2002, *A&A*, 393, 597
 Natta, A., Testi, L., Muzerolle, J., et al. 2004, *A&A*, 424, 603
 Natta, A., Testi, L., & Randich, S. 2006, *A&A*, 452, 245
 Natta, A., Testi, L., Alcalá, J. M., et al. 2014, *A&A*, 569, AA5
 Padoan, P., Kritsuk, A., Norman, M. L., & Nordlund, Å. 2005, *ApJ*, 622, L61
 Rigliaco, E., Natta, A., Randich, S., Testi, L., & Biazzo, K. 2011a, *A&A*, 525, A47
 Rigliaco, E., Natta, A., Randich, S., et al. 2011b, *A&A*, 526, LL6
 Rigliaco, E., Natta, A., Testi, L., et al. 2012, *A&A*, 548, A56
 Rigliaco, E., Pascucci, I., Gorti, U., Edwards, S., & Hollenbach, D. 2013, *ApJ*, 772, 60
 Scholz, A. 2012, *MNRAS*, 420, 1495
 Stelzer, B., Alcalá, J. M., Scholz, A., et al. 2013, *A&A*, 551, AA106
 Valenti, J. A., Basri, G., & Johns, C. M. 1993, *AJ*, 106, 2024
 Vernet, J., Dekker, H., D'Odorico, S., et al. 2011, *A&A*, 536, A105
 Vorobyov, E. I., & Basu, S. 2009, *ApJ*, 703, 922
 White, R. J., & Basri, G. 2003, *ApJ*, 582, 1109
 Wilking, B. A., & Lada, C. J. 1983, *ApJ*, 274, 698
 Wilking, B. A., Greene, T. P., & Meyer, M. R. 1999, *AJ*, 117, 469
 Wilking, B. A., Meyer, M. R., Robinson, J. G., & Greene, T. P. 2005, *AJ*, 130, 1733

Appendix A: Comments on individual objects

Here we report the previous results available in the literature in Table A.1. These are discussed in Sect. 3.3 in comparison with our estimates. In the following, we discuss some peculiar objects in the sample.

A.1. ISO-Oph094

The location of this object on the HRD that we derive is that of a very old PMS object, much older than 100 Myr. However, the spectrum of this object has SNR ~ 0 in the whole VIS arm and

Table A.1. Data available in the literature for the targets included in this work

Object/other name	RA(2000) h :m :s	DEC(2000) ° ' "	SpT	A_V [mag]	References	McClure et al. (2010) classification
ISO–Oph023 / SKS1 / CRBR 2317.3-1925	16:26:18.821	–24:26:10.52	M7.5,M5.5,M7	10.0	1,2,3	Disk
ISO–Oph030 / GY5	16:26:21.528	–24:26:00.96	M5.5,M6,M6	2.8	4,1,3	Disk
ISO–Oph032 / GY3	16:26:21.899	–24:44:39.76	M8,M7.5	0.0	4,3	...
ISO–Oph033 / GY11	16:26:22.269	–24:24:07.06	M8.5,M6.5,M8.5	8.0	5,1,3	...
ISO–Oph037 / LFAM3 / GY21	16:26:23.580	–24:24:39.50	M0,K5	16.1	7,6	Disk/FS
ISO–Oph072 / WL18	16:26:48.980	–24:38:25.24	K6.5	10.4	4	Disk
ISO–Oph087	16:26:58.639	–24:18:34.66
ISO–Oph094	16:27:03.591	–24:20:05.45	M3?	20.1	8	...
ISO–Oph102 / GY204	16:27:06.596	–24:41:48.84	M5.5,M6	0.5	4,3	Disk
ISO–Oph115 / WL11 / GY229	16:27:12.131	–24:34:49.14	M0,M0	11.5	7,6	Disk
ISO–Oph117 / WLY2-32b / GY235	16:27:13.823	–24:43:31.66	M5,K8	7.5	7,6	Disk/FS
ISO–Oph123	16:27:17.590	–24:05:13.70	M3.5	4.4	4	...
ISO–Oph160 / B162737-241756	16:27:37.422	–24:17:54.87	M6	6.0	3	...
ISO–Oph164 / GY310	16:27:38.631	–24:38:39.19	M8.5,M7,M6	5.7	1,2,3	Disk
ISO–Oph165 / GY312	16:27:38.945	–24:40:20.67	M2	15.0	7	Envelope/I
ISO–Oph176 / GY350	16:27:46.291	–24:31:41.19	M6,M6	7.0	3,7	Disk
ISO–Oph193 / B162812-241138	16:28:12.720	–24:11:35.60	M6	7.5	3	...

Notes. Spectral types, extinction, and mass accretion rates determined from the following studies: 1. Wilking et al. (1999); 2. Luhman & Rieke (1999); 3. Natta et al. (2002); 4. Wilking et al. (2005); 5. Comerón et al. (2010); 6. Gatti et al. (2006), 7. McClure et al. (2010, and references therein), 8. Alves de Oliveira et al. (2012)

also has low SNR in the NIR arm. The SpT we have derived is compatible with the highly uncertain estimates by Alves de Oliveira et al. (2012), who suggest that this object has probably a SpT earlier than M3 and strongly extincted ($A_V=20.1$ mag). Also, their near-infrared spectra had very low SNR and their estimates are tentative. Even if we allow for higher values of A_V in our fit, we obtain the same best fit as that we report in this manuscript. As there is no other information available in the literature for these targets from mid-infrared data other than Bontemps et al. (2001), we are not able to further constrain its evolutionary class, which was reported to be Class II using ISO photometry. With the spectra available and the information in our hand, we cannot further constrain the properties of this object. Our classification for this object as subluminescent is also related to the tentative detection of forbidden emission lines in its spectrum. However, given the very low SNR of the continuum of this object, the subtraction of sky lines is not trivial and residuals are present even after careful extraction of the spectrum.

A.2. ISO–Oph102

The value of $\chi^2_{\text{like,red}}$ for the best fit for this object is ~ 12.4 . As discussed in Sect. 2, the spectrum of this target is of very poor quality in the last ~ 100 nm of the VIS arm. We have therefore neglected some points in this region to avoid biases due to the poor quality of the spectrum. Even if the value of $\chi^2_{\text{like,red}}$ is high, the best-fit template reproduces correctly the spectrum in the other features at shorter wavelength and in the NIR. Finally, our estimates are in good agreement with the literature.

A.3. ISO–Oph123

As we mentioned many times, this object is very peculiar and the analysis of its spectrum does not lead to a satisfying estimate of its stellar properties. This object has been studied by Wilking et al. (2005) who reported a SpT of M3.5 with no particular comments, only that there were strong emission lines in

the spectrum. Scholz (2012) has also noted that this object is extremely variable in the near infrared, with variations up to ~ 0.9 mag in K -band. The flux calibration of the spectrum analyzed here is compatible with the 2MASS photometry in J - and H -bands, and it was only correct by a factor 1.12 to account for slit losses to match these bands. The magnitudes at optical wavelengths reported in the literature are, instead, slightly lower than the observed flux of this spectrum. The procedure adopted here for the rest of the targets does not result in a low value of $\chi^2_{\text{like,red}}$ for this target. The best-fit estimate is also probably uncertain as this object seems a very strong accretor, and we discussed that our procedure fails if the target has $L_{\text{acc}}/L_{\star} \gtrsim 0.5$, as could be the case for this object. As the excess due to accretion could significantly change the shape of the continuum, it is not possible to determine the real reddening of the spectrum without considering all the components, such as excess due to accretion or reddening. We tried to fit this spectrum using the procedure by Manara et al. (2013b), as the SNR in the UVB arm, although very low, is not zero. However, this automatic procedure is not able to reproduce the spectrum in the Balmer continuum region without further constraints on some parameters of the fit. We have then constrained the value of A_V to be between ~ 5 mag and ~ 7 mag, as this is the range of values for which the spread of L_{acc} derived from the various emission lines present in the spectrum is minimum. With this constraint and forcing L_{\star} for this object to be that of a 1.2 or 2 Myr old YSO, we obtain a best fit with SpT M5. The accretion rates that would result from the fit of the UV-excess with these parameters are one order of magnitude higher than those derived from the emission lines, however, and would result in a VLMS ($M_{\star} = 0.17 M_{\odot}$) accreting at $\dot{M}_{\text{acc}} \sim 8 \times 10^{-7} M_{\odot}/\text{yr}$. As we show in Fig. C.1, many emission lines in this spectrum show strong absorption features in their profiles, and this could suggest that their real flux is larger. We do not expect the difference with the real flux to be larger than a factor ~ 2 -3, which still is not compatible with the estimates from the UV-excess fit. The profiles of these lines suggest that this ob-

ject might have a powerful jet, but more analyses are needed and are out of the scope of this work.

A.4. *ISO-Oph165*

As reported by McClure et al. (2010), this target is a Class I object. Therefore, its photospheric continuum is strongly extinguished by the envelope that still surrounds the central star and the estimates of L_\star are biased by this. This is the reason why this object appears to be subluminal on the HRD.

**Appendix B: Best fit of observed ρ -Oph spectra
with templates**

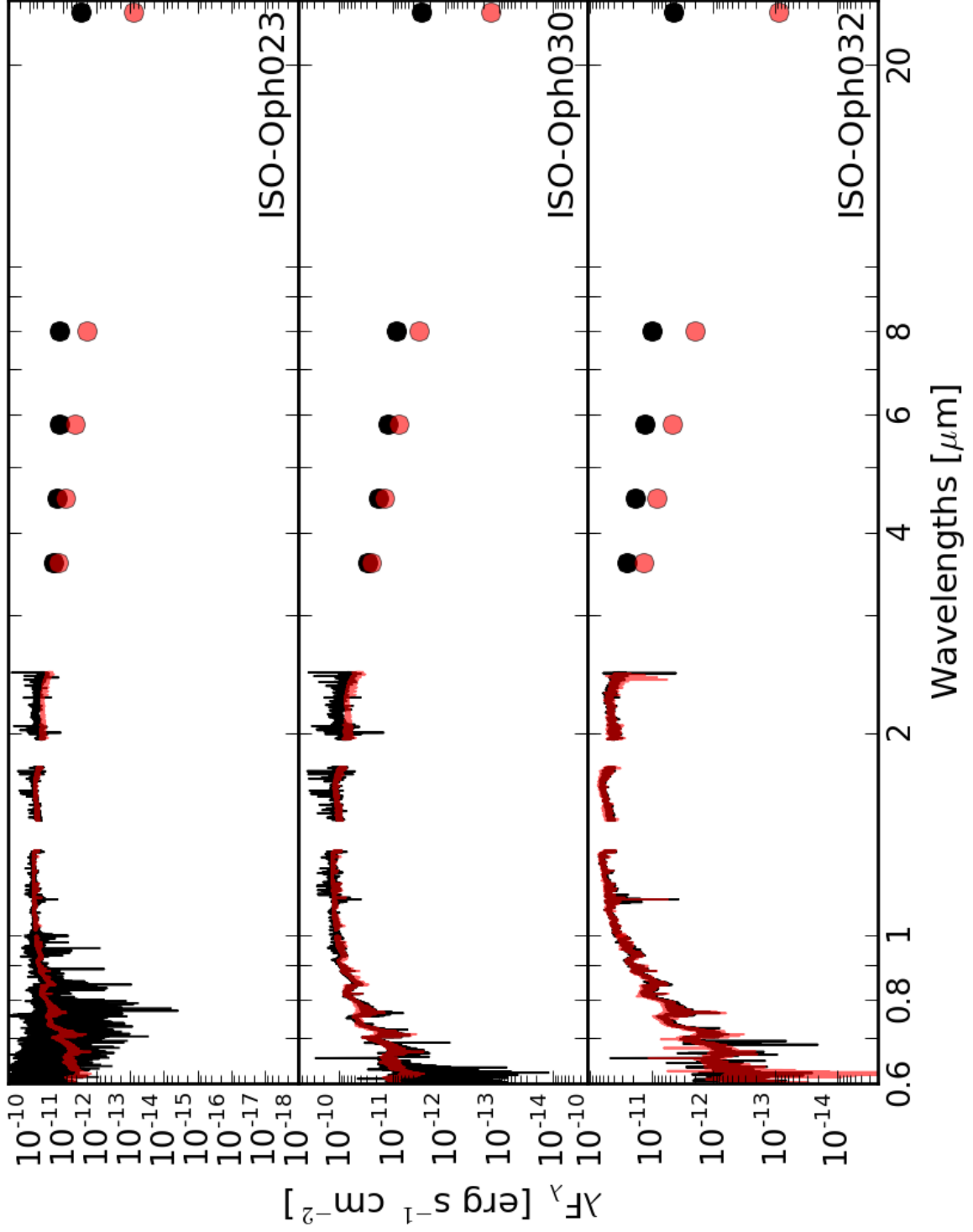


Fig. B.1. Spectra of ρ -Oph targets from 600 to 2450 nm and *Spitzer* photometry up to $24\mu\text{m}$. The extinction-corrected spectra and photometric points for the targets are shown in black. Red lines and points are used for the best-fit template spectrum, which is normalized at $\lambda=1025$ nm to match the extinction-corrected target spectrum. Veiling due to accretion or disk emission is not included.

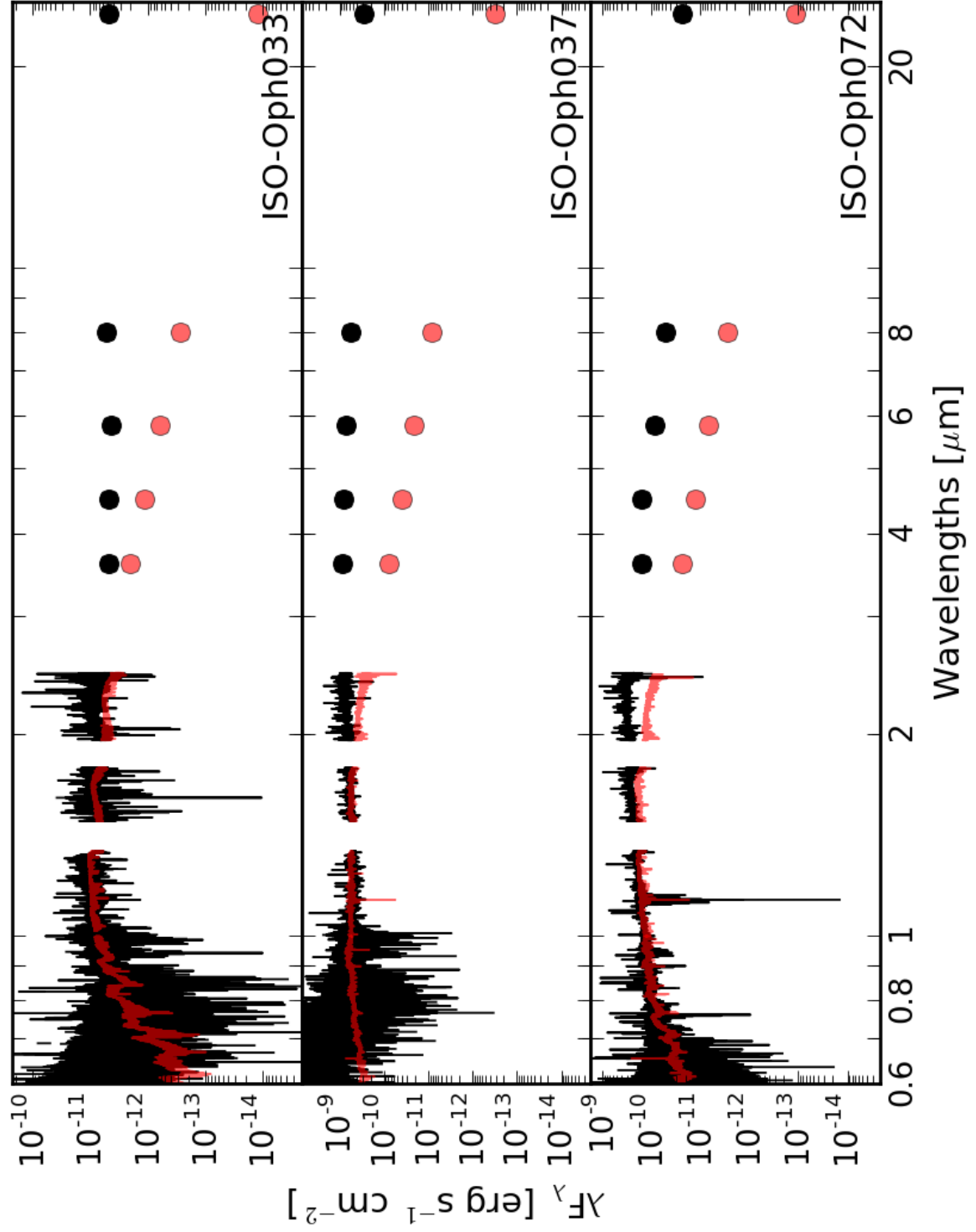


Fig. B.2. Same as Fig. B.1.

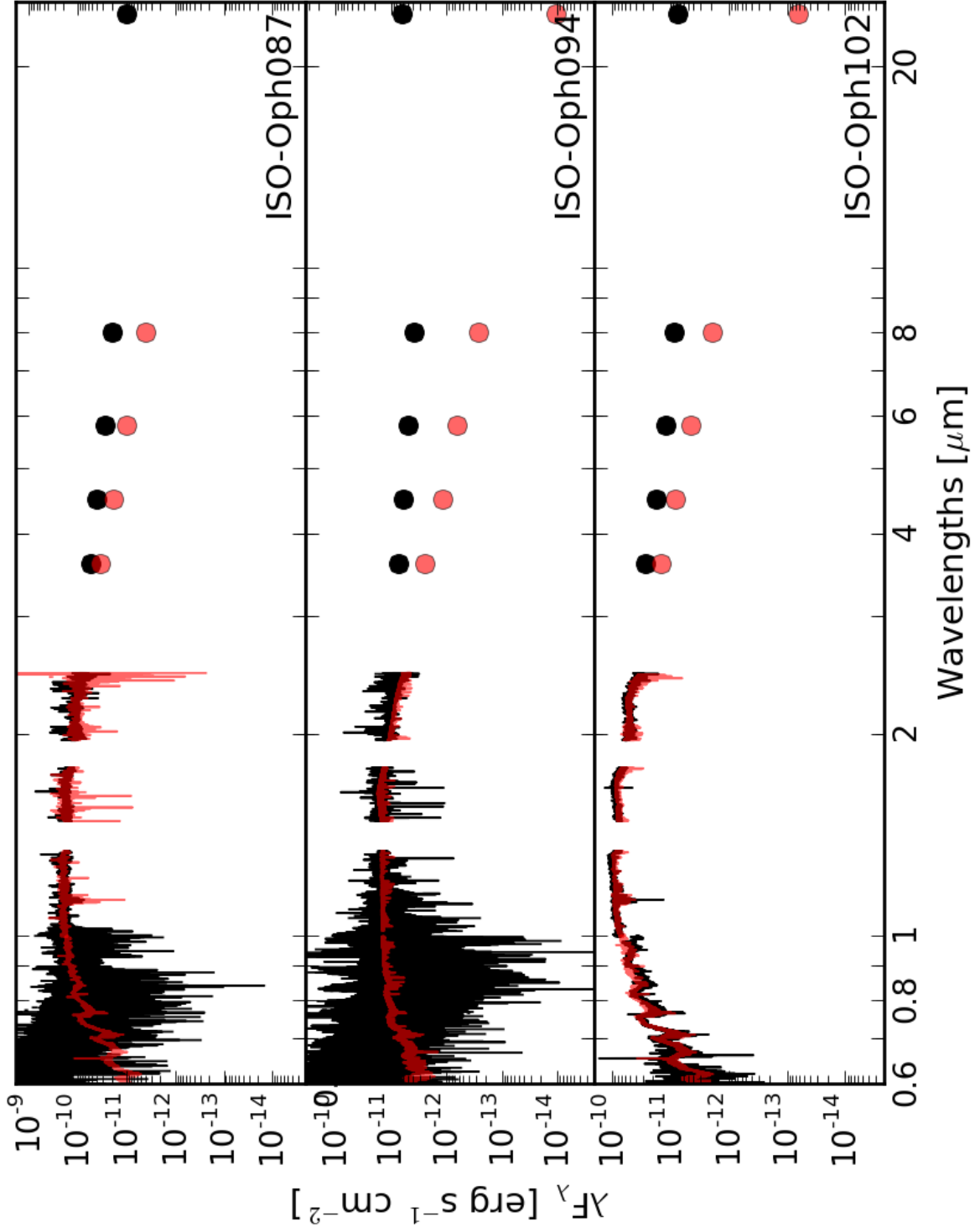


Fig. B.3. Same as Fig. B.1.

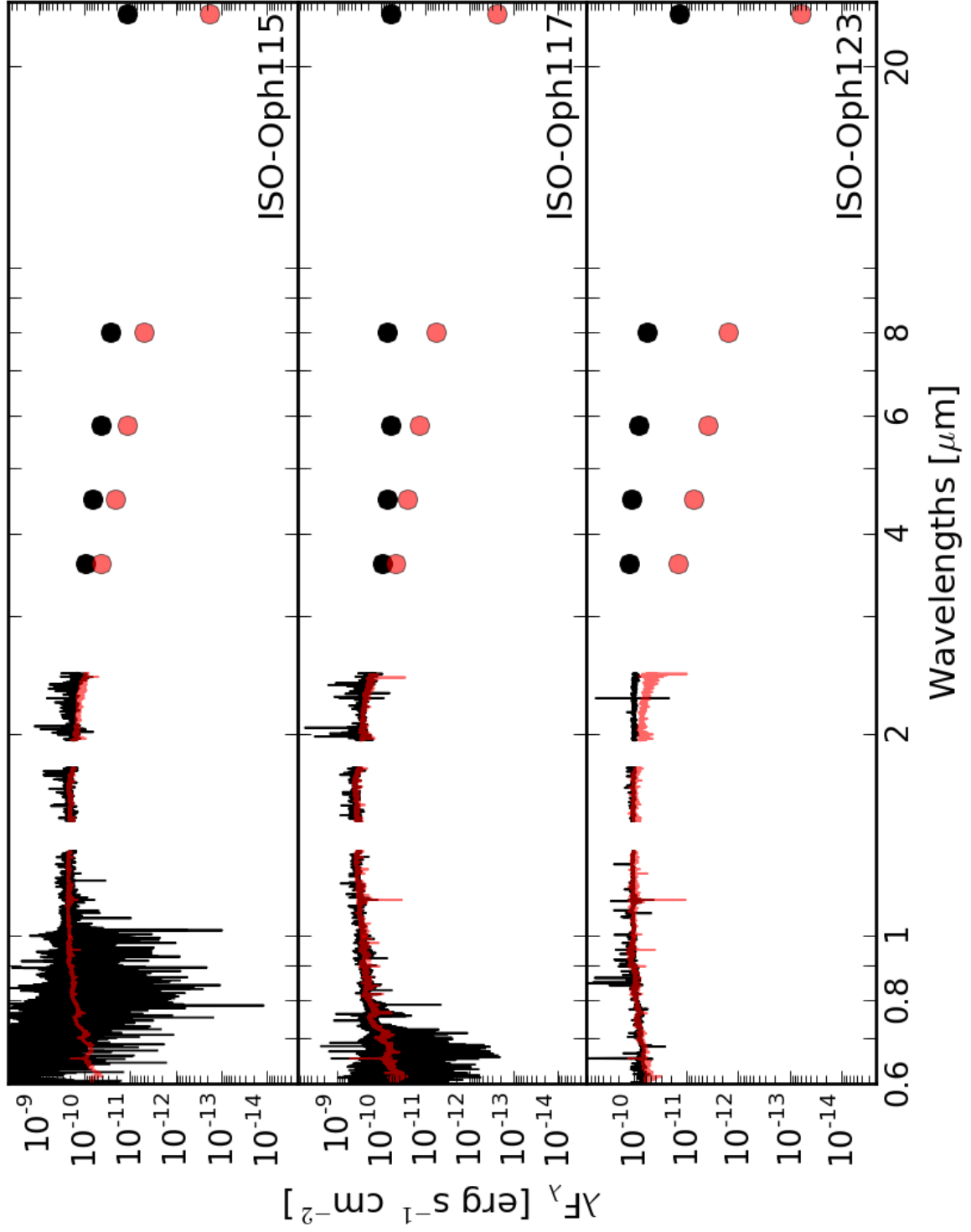


Fig. B.4. Same as Fig. B.1.

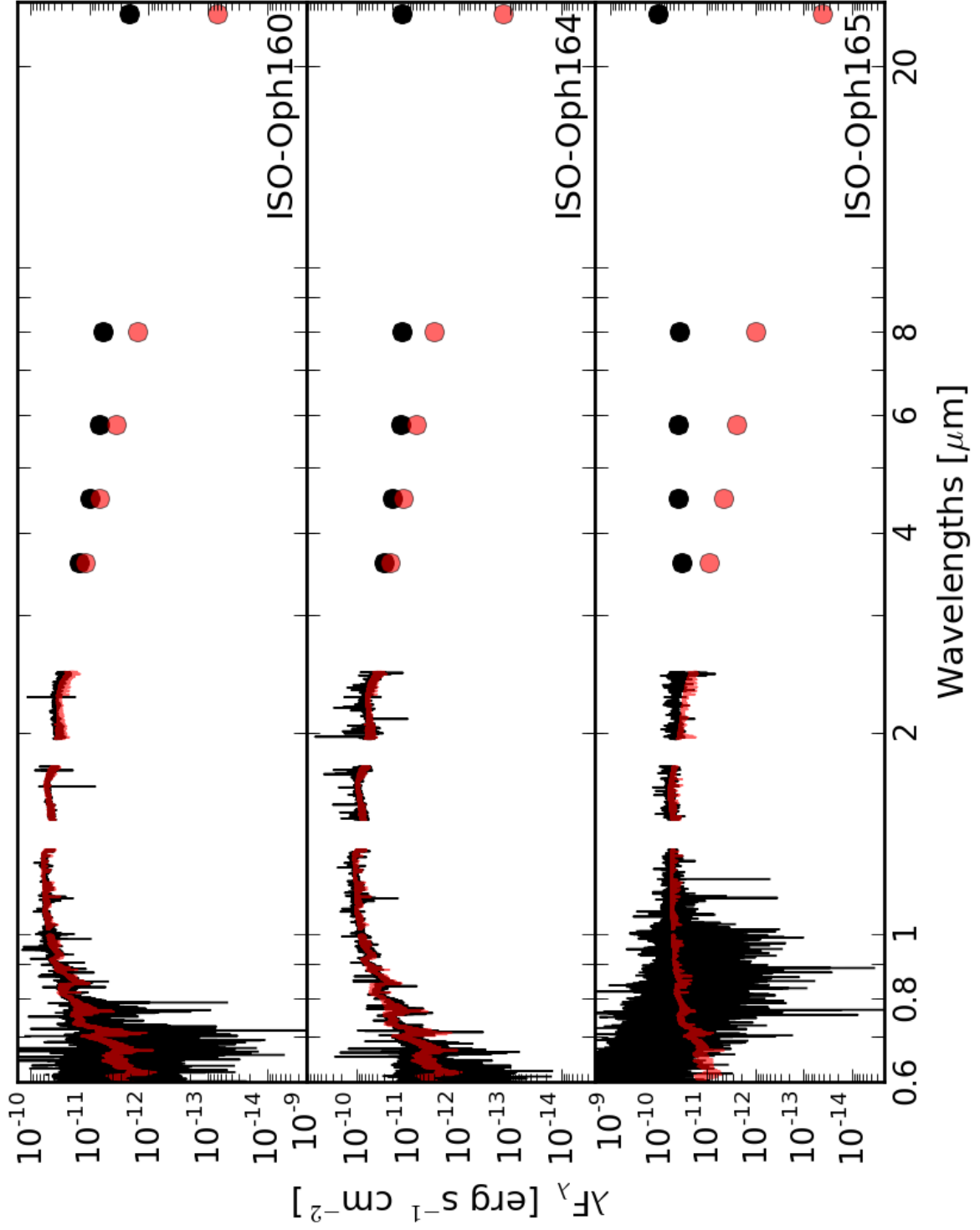


Fig. B.5. Same as Fig. B.1.

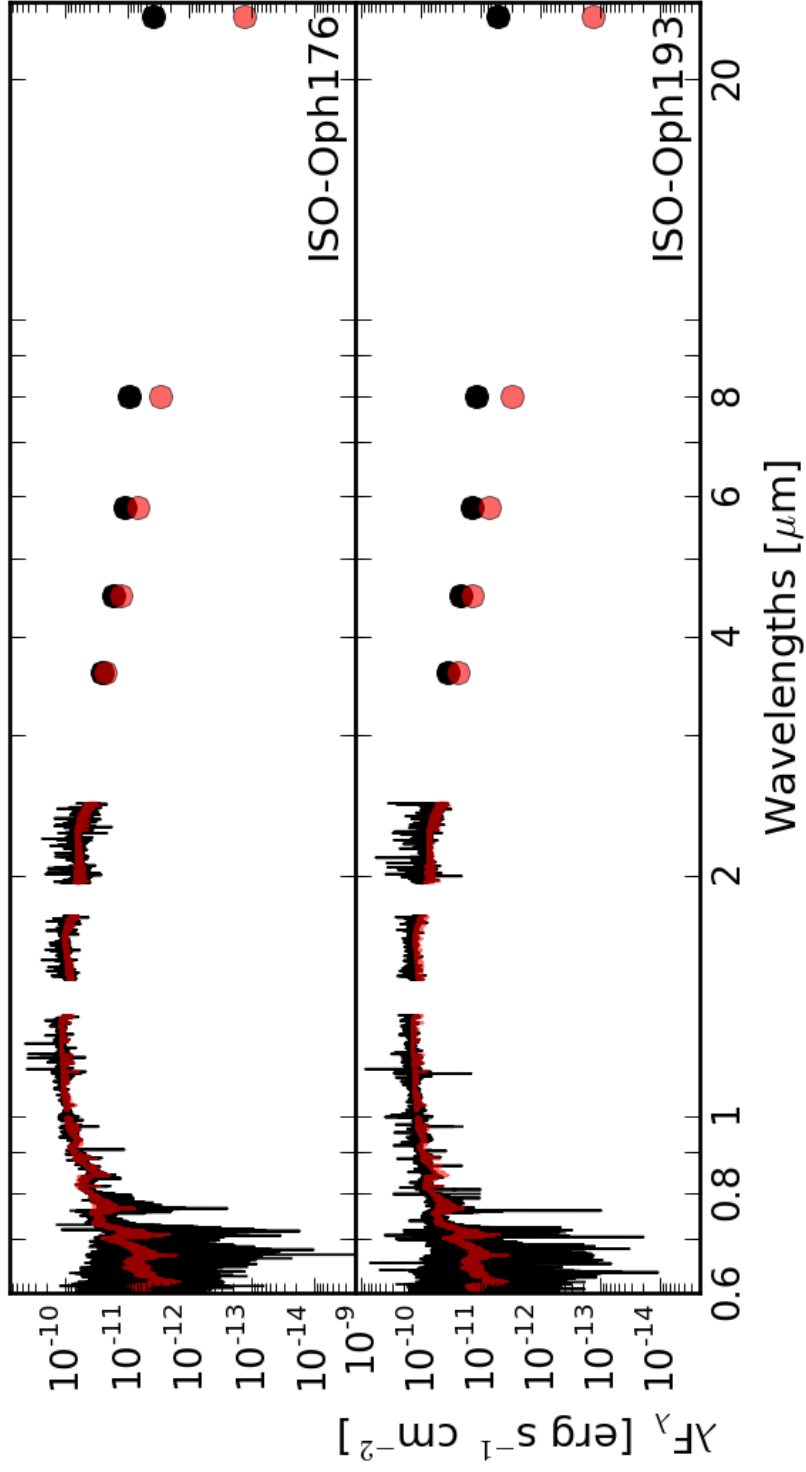


Fig. B.6. Same as Fig. B.1.

Appendix C: Permitted emission line profiles in the X-Shooter spectra

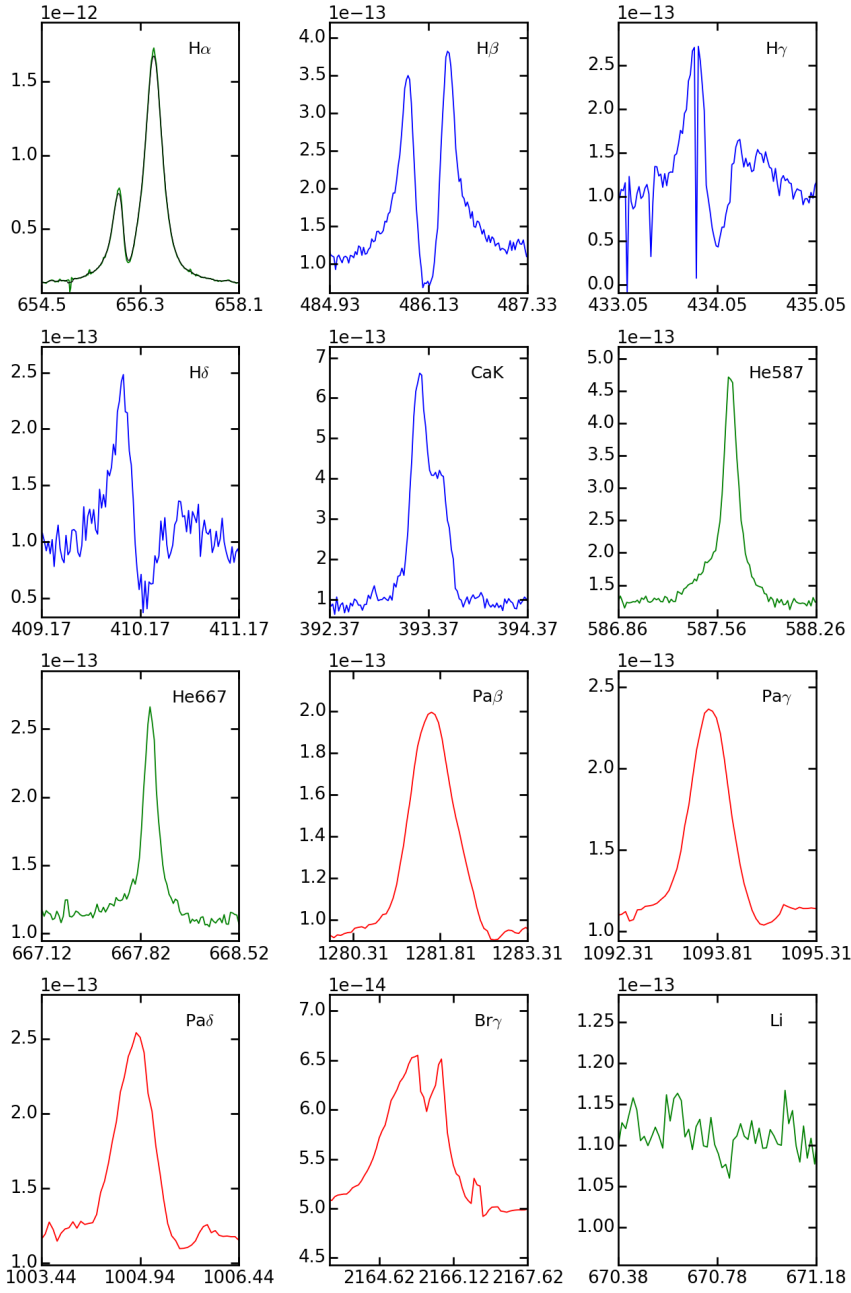


Fig. C.1. Line profiles of permitted transition lines of ISO-Oph123.

Table C.1. Extinction-corrected fluxes and equivalent widths of Balmer, Paschen, and Bracket lines

Object	$f_{\text{H}\alpha}$	$EW_{\text{H}\alpha}$ [nm]	$f_{\text{H}\beta}$	$EW_{\text{H}\beta}$ [nm]	$f_{\text{H}\gamma}$	$EW_{\text{H}\gamma}$ [nm]	$f_{\text{H}\delta}$	$EW_{\text{H}\delta}$ [nm]	$EW_{\text{H}\delta}$ [nm]
ISO-Oph023	10.3 \pm 4.2	-9.472 \pm 3.864	<105.0	...	<175.0	...	<231.0
ISO-Oph030	18.2 \pm 0.3	-8.523 \pm 0.162	1.2 \pm 0.3	-3.303 \pm 0.972	<0.7	...	<0.9
ISO-Oph032	2.460 \pm 0.030	-13.535 \pm 0.165	0.269 \pm 0.018	-7.954 \pm 0.542	0.141 \pm 0.016	-8.077 \pm 0.901	0.105 \pm 0.016	-6.615 \pm 1.003	...
ISO-Oph033	1.3 \pm 0.4	-12.118 \pm 3.614	<20.0	...	<26.9	...	<38.2
ISO-Oph037	3430.0 \pm 795.0	-4.534 \pm 1.052
ISO-Oph072	234.0 \pm 6.2	-14.248 \pm 0.379	45.6 \pm 14.0	-2.297 \pm 0.704	<45.2	...	<72.3
ISO-Oph087	<101.0	...	<2490.0	...	<4540.0	...	<7760.0
ISO-Oph094	<9.2	...	<116.0	...	<168.0	...	<226.0
ISO-Oph102	8.8 \pm 0.3	-4.760 \pm 0.146	0.6 \pm 0.2	-2.400 \pm 0.621	0.8 \pm 0.3	-3.769 \pm 1.273	0.7 \pm 0.3	-2.054 \pm 0.834	...
ISO-Oph115	<408.0	...	<14200.0	...	<47600.0	...	<92700.0
ISO-Oph117	75.9 \pm 8.0	-4.468 \pm 0.472	<42.8	...	<184.0	...	<146.0
ISO-Oph123	81.6 \pm 0.9	-6.068 \pm 0.066	12.0 \pm 0.8	-1.232 \pm 0.080	4.9 \pm 1.1	-0.553 \pm 0.119	3.0 \pm 0.6	-0.377 \pm 0.075	...
ISO-Oph160	8.5 \pm 0.7	-10.546 \pm 0.883	<3.8	...	<7.6	...	<8.9
ISO-Oph164	10.5 \pm 0.4	-6.335 \pm 0.222	2.8 \pm 0.6	-3.133 \pm 0.631	1.5 \pm 0.6	-1.881 \pm 0.724	<1.7
ISO-Oph165	36.0 \pm 22.0	-6.484 \pm 3.966	<1130.0	...	<2860.0	...	<5170.0
ISO-Oph176	0.8 \pm 0.3	-0.728 \pm 0.232
ISO-Oph193	43.7 \pm 2.6	-9.836 \pm 0.592
Object	$f_{\text{Pa}\beta}$	$EW_{\text{Pa}\beta}$ [nm]	$f_{\text{Pa}\gamma}$	$EW_{\text{Pa}\gamma}$ [nm]	$f_{\text{Pa}\delta}$	$EW_{\text{Pa}\delta}$ [nm]	$f_{\text{Br}\gamma}$	$EW_{\text{Br}\gamma}$ [nm]	
ISO-Oph023	0.3 \pm 0.2	-0.039 \pm 0.035	0.4 \pm 0.2	-0.060 \pm 0.032	<1.3	...	0.2 \pm 0.1	-0.053 \pm 0.026	
ISO-Oph030	0.4 \pm 0.2	-0.033 \pm 0.023	0.6 \pm 0.3	-0.051 \pm 0.022	1.1 \pm 0.5	-0.107 \pm 0.049	<0.1	...	
ISO-Oph032	0.069 \pm 0.109	-0.014 \pm 0.022	0.278 \pm 0.137	-0.062 \pm 0.030	<0.13	...	<0.05	...	
ISO-Oph033	<0.1	...	<0.1	...	<0.5	...	<0.0	...	
ISO-Oph037	24.5 \pm 2.0	-0.614 \pm 0.049	23.6 \pm 3.8	-0.468 \pm 0.075	<38.7	...	<1.1	...	
ISO-Oph072	39.5 \pm 0.8	-2.455 \pm 0.052	36.5 \pm 1.1	-2.088 \pm 0.063	21.7 \pm 2.4	-1.485 \pm 0.166	14.1 \pm 0.3	-0.946 \pm 0.022	
ISO-Oph087	<0.9	...	<1.0	...	<10.9	...	<0.4	...	
ISO-Oph094	0.2 \pm 0.1	-0.207 \pm 0.122	<0.3	...	<2.8	...	<0.0	...	
ISO-Oph102	<0.2	...	0.4 \pm 0.2	-0.044 \pm 0.021	<0.3	...	<0.1	...	
ISO-Oph115	3.0 \pm 1.2	-0.144 \pm 0.058	<2.0	...	<20.8	...	<0.6	...	
ISO-Oph117	0.9 \pm 0.8	-0.030 \pm 0.028	0.9 \pm 0.9	-0.031 \pm 0.031	<2.3	...	<0.4	...	
ISO-Oph123	9.0 \pm 0.2	-0.980 \pm 0.020	7.7 \pm 0.4	-0.701 \pm 0.040	7.7 \pm 0.6	-0.660 \pm 0.055	2.1 \pm 0.1	-0.416 \pm 0.018	
ISO-Oph160	1.1 \pm 0.1	-0.238 \pm 0.032	0.9 \pm 0.2	-0.178 \pm 0.046	<0.6	...	0.2 \pm 0.0	-0.101 \pm 0.023	
ISO-Oph164	1.5 \pm 0.2	-0.160 \pm 0.018	4.4 \pm 0.7	-0.368 \pm 0.056	1.9 \pm 0.9	-0.219 \pm 0.101	<0.2	...	
ISO-Oph165	0.5 \pm 0.3	-0.116 \pm 0.069	<0.6	...	<9.0	...	<0.1	...	
ISO-Oph176	<0.3	...	<0.2	...	<0.8	...	<0.1	...	
ISO-Oph193	1.6 \pm 0.6	-0.138 \pm 0.048	1.0 \pm 0.5	-0.076 \pm 0.037	<2.9	...	<0.1	...	

Notes. Fluxes are reported in units of 10^{-14} erg s $^{-1}$ cm $^{-2}$ followed by their errors. Upper limits (3σ) are reported with <.

Table C.2. Extinction-corrected fluxes and equivalent widths of helium and calcium lines

Object	$f_{\text{He}4587.6}$	$EW_{\text{He}4587.6}$ [nm]	$f_{\text{He}4667.8}$	$EW_{\text{He}4667.8}$ [nm]	f_{CaK}	EW_{CaK} [nm]
ISO-Oph023	<28.6	...	<7.6	...	<248.0	...
ISO-Oph030	0.3 ± 0.1	-0.432 ± 0.190	0.2 ± 0.1	-0.141 ± 0.050	<0.7	...
ISO-Oph032	0.054 ± 0.007	-1.162 ± 0.148	0.029 ± 0.006	-0.277 ± 0.060	0.036 ± 0.011	-4.716 ± 1.382
ISO-Oph033	<8.4	...	<1.4	...	<33.2	...
ISO-Oph037	<8500.0	...	<1390.0
ISO-Oph072	<11.0	...	<3.4	...	<99.7	...
ISO-Oph087	<663.0	...	<106.0	...	<9210.0	...
ISO-Oph094	<104.0	...	<9.3	...	<240.0	...
ISO-Oph102	0.6 ± 0.1	-0.875 ± 0.190	0.3 ± 0.0	-0.234 ± 0.038	0.7 ± 0.3	-3.602 ± 1.470
ISO-Oph115	<2380.0	...	<550.0	...	<127000.0	...
ISO-Oph117	<27.1	...	<9.7	...	<192.0	...
ISO-Oph123	5.4 ± 0.3	-0.472 ± 0.025	2.0 ± 0.1	-0.194 ± 0.014	15.6 ± 0.7	-1.872 ± 0.085
ISO-Oph160	<2.4	...	<2.7	...	<24.1	...
ISO-Oph164	0.7 ± 0.2	-1.356 ± 0.462	0.3 ± 0.1	-0.362 ± 0.105	<2.0	...
ISO-Oph165	<569.0	...	<66.2	...	<6960.0	...
ISO-Oph176	<3.4	...	<1.4
ISO-Oph193	<6.9	...	<2.3

Notes. Fluxes are reported in units of 10^{-14} erg s $^{-1}$ cm $^{-2}$ followed by their errors. Upper limits (3σ) are reported with <.

Appendix D: Stellar and accretion parameters by Natta et al. (2006) corrected for the most recent distance estimate**Table D.1.** Properties of ρ -Ophiuci young stellar objects from N06 using distance of 125 pc.

#	Object (ISO#)	Class	$\log L_{\star}$ [L_{\odot}]	$\log T_{\text{eff}}$ [K]	$\log M_{\star}$ [M_{\odot}]	Line	EW(line) [Å]	$\log L_{\text{line}}$ [L_{\odot}]	$\log L_{\text{acc}}$ [L_{\odot}]	$\log \dot{M}_{\text{acc}}$ [M_{\odot}/yr]
1	ISO-Oph001	II	0.16	3.58	0.02	Pa β	<0.7	<-4.36	<-1.93	<-9.01
2	ISO-Oph002	II	-0.21	3.54	-0.24	Pa β	2.8	-4.14	-1.63	-8.55
3	ISO-Oph003	II	-0.13	3.55	-0.19	Pa β	3.9	-3.92	-1.33	-8.28
4	ISO-Oph005	III	0.12	3.58	-0.01	Pa β	<0.5	<-4.57	<-2.21	<-9.27
5	ISO-Oph006	II	0.07	3.58	-0.03	Pa β	19.0	-3.03	-0.12	-7.18
6	ISO-Oph009	II	-1.13	3.48	-0.99	Pa β	<0.3	<-5.84	<-3.94	<-10.46
7	ISO-Oph011	III	-0.29	3.53	-0.31	Pa β	<0.8	<-4.61	<-2.26	<-9.14
8	ISO-Oph012	II	-1.07	3.48	-0.95	Pa β	<0.2	<-6.05	<-4.23	<-10.75
9	ISO-Oph013	II	-0.26	3.54	-0.28	Pa β	2.1	-4.31	-1.86	-8.76
10	ISO-Oph014	III	0.01	3.57	-0.09	Pa β	<0.5	<-4.71	<-2.40	<-9.41
11	ISO-Oph016	III	0.49	3.66	0.20	Pa β	-5.7
12	ISO-Oph017	II	0.54	3.67	0.22	Pa β	<0.8	<-4.08	<-1.55	<-8.81
13	ISO-Oph018	III	0.06	3.58	-0.04	Pa β	<0.5	<-4.67	<-2.36	<-9.41
14	ISO-Oph019	II	0.55	3.67	0.23	Pa β	<0.9	<-3.97	<-1.40	<-8.67
15	ISO-Oph020	II	-0.02	3.56	-0.11	Pa β	1.2	-4.30	-1.85	-8.85
16	ISO-Oph023	II	-1.85	3.45	-1.36	Pa β	1.8	-5.63	-3.65	-10.09
17	ISO-Oph024	II	0.26	3.60	0.07	Pa β	8.9	-3.21	-0.36	-7.47
18	ISO-Oph026	II	-0.48	3.52	-0.48	Pa β	2.4	-4.27	-1.80	-8.58
19	ISO-Oph028	III	0.36	3.61	0.12	Pa β	<0.6	<-4.33	<-1.89	<-9.03
20	ISO-Oph030	II	-1.42	3.47	-1.14	Pa β	0.3	-6.03	-4.20	-10.68
21	ISO-Oph032	II	-1.71	3.45	-1.29	Pa β	0.4	-6.13	-4.34	-10.79
22	ISO-Oph033	II	-3.26	3.33	nan	Pa β	<0.7	<-7.22	<-5.82	<nan
23	ISO-Oph035	II	-1.17	3.48	-1.01	Pa β	-0.6
24	ISO-Oph036	II	0.70	3.68	0.31	Pa β	0.7	-3.92	-1.34	-8.64
25	ISO-Oph037	II	-0.79	3.50	-0.78	Pa β	3.0	-4.62	-2.28	-8.87
26	ISO-Oph038	II	0.00	3.56	-0.10	Pa β	<0.3	<-4.87	<-2.63	<-9.64
27	ISO-Oph039	II	0.99	3.71	0.37	Pa β	<0.5	<-3.87	<-1.26	<-8.54
28	ISO-Oph040	II	0.53	3.66	0.22	Pa β	12.7	-2.83	0.15	-7.11
29	ISO-Oph041	II	-0.61	3.51	-0.61	Pa β	<0.3	<-5.42	<-3.36	<-10.06
30	ISO-Oph043	II	0.01	3.57	-0.09	Pa β	<1.0	<-4.40	<-1.99	<-9.00
31	ISO-Oph044	III	-0.15	3.55	-0.21	Pa β	<0.7	<-4.69	<-2.38	<-9.32
32	ISO-Oph046	II	-0.11	3.55	-0.18	Pa β	16.5	-3.29	-0.48	-7.43
33	ISO-Oph047	III	-0.40	3.53	-0.41	Bry	<1.0	<-5.15	<-1.73	<-8.55
34	ISO-Oph051	II	-0.67	3.51	-0.66	Pa β	<0.4	<-5.39	<-3.33	<-9.99
35	ISO-Oph052	II	-0.79	3.50	-0.77	Pa β	5.9	-4.28	-1.83	-8.42
36	ISO-Oph053	II	-0.81	3.50	-0.79	Pa β	<0.3	<-5.60	<-3.62	<-10.20
37	ISO-Oph055	III	-1.82	3.45	-1.34	Pa β	<1.0	<-5.90	<-4.02	<-10.46
38	ISO-Oph056	II	-0.56	3.51	-0.55	Pa β	<0.5	<-5.13	<-2.98	<-9.71
39	ISO-Oph058	III	0.58	3.67	0.25	Pa β	<0.5	<-4.25	<-1.78	<-9.05
40	ISO-Oph059a	II	-0.40	3.53	-0.41	Bry	<0.6	<-5.37	<-1.93	<-8.75
41	ISO-Oph059b	II	-0.29	3.53	-0.31	Pa β	<3.0	<-4.05	<-1.51	<-8.39
42	ISO-Oph062	II	0.55	3.67	0.23	Pa β	1.4	-3.79	-1.15	-8.41
43	ISO-Oph063	II	-0.73	3.50	-0.73	Pa β	<0.3	<-5.53	<-3.52	<-10.13
44	ISO-Oph064	III	0.04	3.57	-0.04	Pa β	<0.7	<-4.51	<-2.14	<-9.20
45	ISO-Oph065	I	-1.35	3.47	-1.10	Pa β	<10.0	<-4.56	<-2.20	<-8.69
46	ISO-Oph066	III	-0.67	3.51	-0.66	Pa β	<0.8	<-5.01	<-2.81	<-9.47
47	ISO-Oph067	II	0.21	3.59	0.04	Pa β	10.0	-3.24	-0.41	-7.49
48	ISO-Oph068	II	0.30	3.60	0.09	Pa β	0.6	-4.32	-1.87	-8.99
49	ISO-Oph069	III	-0.95	3.49	-0.88	Pa β	<0.4	<-5.55	<-3.55	<-10.10
50	ISO-Oph070	II	-3.34	3.32	nan	Bry	<1.2	<-6.80	<-3.22	<nan
51	ISO-Oph072	II	-0.86	3.49	-0.83	Pa β	36.0	-3.55	-0.83	-7.39
52	ISO-Oph073	III	0.57	3.67	0.24	Pa β	<0.4	<-4.32	<-1.88	<-9.15
53	ISO-Oph074	III	-0.25	3.54	-0.28	Pa β	-1.5
54	ISO-Oph075	II	-0.97	3.49	-0.89	Bry	<3.9	<-4.76	<-1.39	<-7.93
55	ISO-Oph076	II	-0.76	3.50	-0.75	Bry	<3.0	<-4.70	<-1.33	<-7.93

Table D.1. Continued.

#	Object (ISO#)	Class	$\log L_{\star}$ [L_{\odot}]	$\log T_{\text{eff}}$ [K]	$\log M_{\star}$ [M_{\odot}]	Line	EW(line) [Å]	$\log L_{\text{line}}$ [L_{\odot}]	$\log L_{\text{acc}}$ [L_{\odot}]	$\log \dot{M}_{\text{acc}}$ [M_{\odot}/yr]
56	ISO-Oph078	II	0.20	3.59	0.03	Pa β	<0.4	<-4.62	<-2.29	<-9.37
57	ISO-Oph079	II	-1.52	3.46	-1.19	Pa β	<3.0	<...	<...	<...
58	ISO-Oph082	III	-1.99	3.44	-1.43	Pa β	<2.0	<-5.71	<-3.77	<-10.19
59	ISO-Oph083	II	-0.04	3.56	-0.12	Pa β	4.5	-3.78	-1.14	-8.13
60	ISO-Oph084a	II	-1.27	3.47	-1.06	Pa β	<5.0	<-99.00	<-99.00	<-99.00
61	ISO-Oph084b	II	-1.27	3.47	-1.06	Bry	<0.2	<-6.48	<-2.93	<-9.43
62	ISO-Oph086	II	-0.60	3.51	-0.59	Pa β	<0.8	<-5.00	<-2.79	<-9.50
63	ISO-Oph087	II	-1.10	3.48	-0.97	Pa β	2.4	-4.90	-2.67	-9.18
64	ISO-Oph088a	II	0.38	3.62	0.13	Pa β	10.5	-3.05	-0.15	-7.30
65	ISO-Oph088b	II	0.41	3.62	0.14	Pa β	7.0	-3.18	-0.33	-7.48
66	ISO-Oph089a	II	-0.87	3.49	-0.83	Pa β	<0.5	<-5.39	<-3.33	<-9.89
67	ISO-Oph089b	II	-0.86	3.49	-0.83	Bry	<0.7	<-5.67	<-2.21	<-8.77
68	ISO-Oph091	III	0.64	3.68	0.28	Pa β	-0.9
69	ISO-Oph092	II	0.91	3.70	0.35	Pa β	8.4	-2.75	0.26	-7.02
70	ISO-Oph093a	II	-0.51	3.52	-0.51	Pa β	<20.0	<-99.00	<-99.00	<-99.00
71	ISO-Oph093b	II	-0.51	3.52	-0.51	Bry	<0.7	<-5.15	<-1.73	<-8.49
72	ISO-Oph094	II	-1.95	3.44	-1.41	Pa β	5.0	-5.33	-3.25	-9.67
73	ISO-Oph095	II	0.11	3.58	-0.02	Pa β	<0.6	<-4.55	<-2.18	<-9.24
74	ISO-Oph096	III	-0.47	3.52	-0.46	Pa β	-0.9
75	ISO-Oph097	III	-0.29	3.53	-0.31	Pa β	-1.1
76	ISO-Oph098	II	-0.06	3.56	-0.14	Pa β	<0.7	<-4.62	<-2.28	<-9.26
77	ISO-Oph100	III	-1.76	3.45	-1.32	Bry	<0.7	<-6.21	<-2.69	<-9.14
78	ISO-Oph102	II	-1.43	3.47	-1.14	Pa β	2.0	-5.22	-3.09	-9.57
79	ISO-Oph103	II	0.43	3.63	0.16	Pa β	<0.6	<...	<...	<...
80	ISO-Oph104	III	-1.36	3.47	-1.11	Bry	<0.7	<-5.87	<-2.39	<-8.87
81	ISO-Oph105	II	0.38	3.62	0.13	Pa β	1.7	-3.81	-1.18	-8.33
82	ISO-Oph106	II	-0.49	3.52	-0.48	Pa β	<1.0	<-4.82	<-2.55	<-9.33
83	ISO-Oph107	II	-0.58	3.51	-0.57	Pa β	<1.3	<...	<...	<...
84	ISO-Oph108	I	4.14	4.47	1.14	Bry	1.3	-1.68	1.39	-6.60
85	ISO-Oph109	III	-0.38	3.53	-0.39	Bry	<0.5	<-5.19	<-1.77	<-8.60
86	ISO-Oph110	II	0.50	3.66	0.20	Pa β	<0.3	<-4.41	<-2.00	<-9.24
87	ISO-Oph111	III	-0.62	3.51	-0.61	Pa β	<1.0	<-4.93	<-2.70	<-9.39
88	ISO-Oph112	II	0.29	3.60	0.08	Pa β	17.9
89	ISO-Oph113a	III	-0.21	3.54	-0.24	Pa β	-4.0	-99.00	-99.00	-99.00
90	ISO-Oph113b	III	-0.21	3.54	-0.24	Bry	-5.6	-99.00	-99.00	-99.00
91	ISO-Oph114	III	0.92	3.71	0.36	Pa β	<8.0	<...	<...	<...
92	ISO-Oph115	II	-1.15	3.48	-1.00	Pa β	2.7	-4.91	-2.68	-9.19
93	ISO-Oph116	II	0.12	3.58	-0.02	Pa β	<1.0	<-4.32	<-1.87	<-8.93
94	ISO-Oph117	II	-0.48	3.52	-0.47	Pa β	2.4	-4.44	-2.03	-8.82
95	ISO-Oph118	II	-0.38	3.53	-0.39	Pa β	<20.0	<...	<...	<...
96	ISO-Oph119	II	-0.38	3.53	-0.39	Bry	<0.7	<-5.05	<-1.64	<-8.47
97	ISO-Oph120	II	-0.35	3.53	-0.36	Pa β	<2.5	<-4.33	<-1.89	<-8.74
98	ISO-Oph121a	II	-0.17	3.55	-0.22	Pa β	<0.6	<-4.76	<-2.48	<-9.41
99	ISO-Oph121b	II	0.36	3.61	0.12	Pa β	<0.5	<-4.40	<-1.99	<-9.13
100	ISO-Oph122	II	-1.20	3.48	-1.02	Pa β	<10.0	<...	<...	<...
101	ISO-Oph123	II	-1.31	3.47	-1.08	Pa β	21.9	-4.10	-1.57	-8.06
102	ISO-Oph124	II	-0.24	3.54	-0.27	Pa β	<10.0	<...	<...	<...
103	ISO-Oph125	III	1.97	3.99	0.50	Pa β	<20.0	<...	<...	<...
104	ISO-Oph126	III	-0.12	3.55	-0.19	Pa β	<0.9	<-4.56	<-2.20	<-9.15
105	ISO-Oph127	II	-0.19	3.54	-0.23	Bry	<0.0	<...	<...	<...
106	ISO-Oph128	II	0.27	3.60	0.08	Pa β	<0.4	<-4.58	<-2.23	<-9.34
107	ISO-Oph129	II	0.06	3.58	-0.04	Pa β	<30.0	<...	<...	<...
108	ISO-Oph130	III	-0.07	3.56	-0.15	Pa β	-0.8
109	ISO-Oph132	II	0.57	3.67	0.24	Pa β	<0.9	<-4.01	<-1.46	<-8.73
110	ISO-Oph133	III	0.23	3.59	0.06	Pa β	<0.9	<-4.28	<-1.83	<-8.93
111	ISO-Oph134	I	2.17	4.11	0.56	Pa β	<12.0	<...	<...	<...
112	ISO-Oph135	III	0.31	3.61	0.10	Pa β	-1.3
113	ISO-Oph136	III	-1.28	3.47	-1.06	Pa β	<0.9	<...	<...	<...
114	ISO-Oph138	II	-1.84	3.45	-1.36	Pa β	<1.0	<-5.95	<-4.09	<-10.53
115	ISO-Oph139a	II	-1.01	3.48	-0.92	Bry	<2.8	<-4.97	<-1.57	<-8.11

Table D.1. Continued.

#	Object (ISO#)	Class	$\log L_{\star}$ [L_{\odot}]	$\log T_{\text{eff}}$ [K]	$\log M_{\star}$ [M_{\odot}]	Line	EW(line) [Å]	$\log L_{\text{line}}$ [L_{\odot}]	$\log L_{\text{acc}}$ [L_{\odot}]	$\log \dot{M}_{\text{acc}}$ [M_{\odot}/yr]
116	ISO-Oph139b	II	-1.01	3.48	-0.91	Pa β	<6.0	<-99.00	<-99.00	<-99.00
117	ISO-Oph140	II	0.42	3.63	0.15	Pa β	3.7	-3.51	-0.77	-7.93
118	ISO-Oph141	I	2.08	4.07	0.53	Bry	0.9	-3.11	0.10	-7.52
119	ISO-Oph142	II	-0.04	3.56	-0.12	Pa β	<0.5	<-4.72	<-2.42	<-9.41
120	ISO-Oph143	I	0.69	3.68	0.30	Bry	1.8	-3.74	-0.47	-7.77
121	ISO-Oph144	II	-0.08	3.56	-0.15	Pa β	<1.4	<-4.32	<-1.88	<-8.85
122	ISO-Oph145	I	0.06	3.58	-0.04	Bry	2.0	-4.02	-0.71	-7.77
123	ISO-Oph146	III	-0.41	3.52	-0.42	Bry	<0.9	<-4.97	<-1.57	<-8.39
124	ISO-Oph147	II	0.51	3.66	0.21	Pa β	<0.5	<-4.31	<-1.86	<-9.11
125	ISO-Oph148	III	-0.36	3.53	-0.36	Pa β	<0.5	<-5.00	<-2.80	<-9.64
126	ISO-Oph149	III	-0.11	3.55	-0.18	Pa β	-0.9
127	ISO-Oph151	II	-0.43	3.52	-0.43	Pa β	<0.5	<-5.08	<-2.91	<-9.72
128	ISO-Oph152	III	0.04	3.57	-0.04	Pa β	<2.0	<-4.07	<-1.53	<-8.59
129	ISO-Oph153	III	-1.55	3.46	-1.21	Bry	<0.0	<...	<...	<...
130	ISO-Oph154	II	0.07	3.58	-0.03	Pa β	<1.0	<-4.38	<-1.95	<-9.01
131	ISO-Oph155	II	0.57	3.67	0.24	Pa β	4.0	-3.30	-0.49	-7.76
132	ISO-Oph156	III	-0.77	3.50	-0.77	Pa β	<0.4	<-5.43	<-3.38	<-9.98
133	ISO-Oph157	III	-1.10	3.48	-0.97	Bry	<1.0	<-5.76	<-2.29	<-8.80
134	ISO-Oph158	III	-1.59	3.46	-1.23	Pa β	<1.0	<-5.74	<-3.81	<-10.27
135	ISO-Oph159	I	0.16	3.58	0.01	Bry	<0.0	<...	<...	<...
136	ISO-Oph160	II	-1.73	3.45	-1.30	Pa β	3.3	-5.26	-3.15	-9.60
137	ISO-Oph161	II	-0.01	3.56	-0.11	Bry	<0.8	<-4.67	<-1.30	<-8.30
138	ISO-Oph163	II	0.26	3.60	0.07	Pa β	2.0	-3.87	-1.27	-8.37
139	ISO-Oph164	II	-1.47	3.46	-1.16	Pa β	0.8	-5.63	-3.66	-10.13
140	ISO-Oph165	II	-1.34	3.47	-1.10	Pa β	9.6	-4.56	-2.20	-8.69
141	ISO-Oph166	II	0.22	3.59	0.05	Pa β	3.3	-3.64	-0.95	-8.05
142	ISO-Oph167	I	2.27	4.14	0.58	Pa β	<4.0	<-2.01	<1.27	<-6.43
143	ISO-Oph168	II	0.11	3.58	-0.02	Pa β	1.3	-4.19	-1.69	-8.75
144	ISO-Oph169	III	-0.26	3.54	-0.29	Pa β	-0.7
144	ISO-Oph169	III	-0.77	3.50	-0.76	Pa β	<0.9	<-5.06	<-2.88	<-9.48
145	ISO-Oph169	III	-0.26	3.54	-0.29	Pa β	-0.7
145	ISO-Oph169	III	-0.77	3.50	-0.76	Pa β	<0.9	<-5.06	<-2.88	<-9.48
146	ISO-Oph170	II	-3.34	3.32	nan	Pa β	<3.0	<-6.68	<-5.09	<nan
147	ISO-Oph171	II	-0.78	3.50	-0.77	Pa β	<4.0	<...	<...	<...
148	ISO-Oph172	II	-0.60	3.51	-0.59	Pa β	<1.0	<-4.91	<-2.68	<-9.38
149	ISO-Oph173	III	-0.21	3.54	-0.25	Pa β	<3.0	<...	<...	<...
150	ISO-Oph174	III	-0.96	3.49	-0.89	Pa β	-0.7
151	ISO-Oph175	II	-1.86	3.45	-1.36	Pa β	15.7	-4.76	-2.47	-8.91
152	ISO-Oph176a	II	-1.22	3.47	-1.03	Pa β	<0.5	<-5.65	<-3.68	<-10.18
153	ISO-Oph176b	II	-1.21	3.48	-1.02	Bry	<0.6	<-6.02	<-2.52	<-9.02
154	ISO-Oph177	II	-0.43	3.52	-0.43	Pa β	<0.4	<-5.13	<-2.97	<-9.78
155	ISO-Oph178	II	-0.73	3.50	-0.73	Pa β	2.0	-4.72	-2.41	-9.03
156	ISO-Oph179	III	-0.88	3.49	-0.84	Bry	<0.7	<-5.68	<-2.21	<-8.77
157	ISO-Oph180	III	0.31	3.61	0.10	Pa β	-6.3
158	ISO-Oph181	III	-1.30	3.47	-1.07	Pa β	-5.5
159	ISO-Oph182	I	0.22	3.59	0.05	Bry	5.4	-3.41	-0.17	-7.26
160	ISO-Oph183	III	-0.18	3.54	-0.23	Pa β	<0.7	<-4.72	<-2.42	<-9.34
161	ISO-Oph184	III	0.22	3.59	0.05	Pa β	-0.7
162	ISO-Oph185	II	-1.08	3.48	-0.96	Pa β	<0.2	<-5.96	<-4.11	<-10.62
163	ISO-Oph186	III	-1.13	3.48	-0.98	Pa β	<1.5	<-5.16	<-3.02	<-9.53
164	ISO-Oph187	II	-0.56	3.51	-0.55	Pa β	5.6	-4.12	-1.61	-8.34
165	ISO-Oph188	III	-0.17	3.54	-0.22	Pa β	-0.5
166	ISO-Oph189	III	-0.86	3.49	-0.83	Pa β	<1.5	<-4.94	<-2.72	<-9.28
167	ISO-Oph190	II	-1.65	3.46	-1.26	Pa β	<5.0	<...	<...	<...
168	ISO-Oph191	III	-0.03	3.56	-0.12	Pa β	<0.5	<-4.74	<-2.45	<-9.44
169	ISO-Oph192	III	-1.06	3.48	-0.94	Pa β	<2.0	<-4.98	<-2.77	<-9.29
170	ISO-Oph193	II	-1.22	3.47	-1.03	Pa β	1.8	-5.20	-3.08	-9.58
171	ISO-Oph194	II	-0.73	3.50	-0.73	Pa β	<0.5	<-5.30	<-3.21	<-9.83
172	ISO-Oph195	II	-0.10	3.55	-0.17	Pa β	0.8	-4.53	-2.17	-9.13
173	ISO-Oph196	II	-0.67	3.51	-0.66	Pa β	3.2	-4.44	-2.03	-8.70

Table D.1. Continued.

#	Object (ISO#)	Class	$\log L_{\star}$ [L_{\odot}]	$\log T_{\text{eff}}$ [K]	$\log M_{\star}$ [M_{\odot}]	Line	EW(line) [Å]	$\log L_{\text{line}}$ [L_{\odot}]	$\log L_{\text{acc}}$ [L_{\odot}]	$\log \dot{M}_{\text{acc}}$ [M_{\odot}/yr]
174	ISO–Oph197	III	-1.11	3.48	-0.97	Pa β	<1.0	<-5.29	<-3.19	<-9.71
175	ISO–Oph198	III	0.73	3.69	0.31	Pa β	<0.4	<-4.12	<-1.60	<-8.90
176	ISO–Oph199	II	-0.13	3.55	-0.19	Pa β	1.7	-4.23	-1.75	-8.70

M_{\star} and age are derived using the evolutionary tracks of Baraffe et al. (1998) and assuming a single isochrone at 1 Myr as explained in Rigliaco et al. (2011a).